2024-05-01

Laser Powder Directed Energy Deposition (LP-DED) Inconel 718: Laser Power and Heat Treatment Effect on Microstructure and Mechanical Properties

Dana Victoria Godinez
University of Texas at El Paso

Recommended Citation

Godinez, Dana Victoria, "Laser Powder Directed Energy Deposition (LP-DED) Inconel 718: Laser Power and Heat Treatment Effect on Microstructure and Mechanical Properties" (2024). *Open Access Theses & Dissertations*. 4098.
https://scholarworks.utep.edu/open_etd/4098

LASER POWDER DIRECTED ENERGY DEPOSITION (LP-DED) INCONEL 718: LASER POWER AND HEAT TREATMENT EFFECTS ON MICROSTRUCTURE AND MECHANICAL PROPERTIES

DANA VICTORIA GODINEZ

Master's Program in Metallurgical and Materials Engineering

APPROVED:

Francisco Medina, Ph.D., Chair

Ryan Wicker, Ph.D.

Binata Joddar, Ph.D.

Stephen L. Crites, Jr., Ph.D.
Dean of the Graduate School

DEDICATION

I dedicate this work to my family, friends, and Diego for their endless support, patience, and love throughout this last year. Thank you for always believing in me and sharing your strength through hard times.

LASER POWDER DIRECTED ENERGY DEPOSITION (LP-DED) INCONEL 718: LASER POWER AND HEAT TREATMENT EFFECTS ON MICROSTRUCTURE AND MECHANICAL PROPERTIES

by

DANA VICTORIA GODINEZ, B.S.M.M.E.

THESIS

Presented to the Faculty of the Graduate School of

The University of Texas at El Paso

in Partial Fulfillment

of the Requirements

for the Degree of

MASTER OF SCIENCE

Department of Metallurgy and Materials Engineering

THE UNIVERSITY OF TEXAS AT EL PASO

May 2024

ACKNOWLEDGEMENTS

I want to express my sincere appreciation to the Keck Center for 3D Innovation at UTEP for their invaluable support throughout this research project. To my mentors, Frank, Edel, and Kurtis, thank you for providing me with such enriching learning experiences. Thanks to the wonderful people there, my time at the Keck Center has been filled with positivity and growth. To my peers, I'm grateful for your guidance and inspiration every day. Additionally, I thank the National Aeronautics and Space Administration (NASA) for their generous funding and ongoing support of our research efforts. Lastly, I want to thank Paul and Colton for their willingness to listen and share their knowledge at all times.

ABSTRACT

This study examines the microstructure and mechanical properties (tensile, hardness, and fatigue endurance) of laser powder-directed energy deposition (LP-DED) printed specimens with varying deposition parameters. Five samples with power inputs ranging from 350 to 2620W, all of similar thicknesses, were evaluated to enable a direct comparison. The varying specimens were heat treated, including stress relief, hot isostatic pressing, solution, and two-step aging. The resulting microstructures and their corresponding hardness values were compared at each heat treatment stage. The fully heat-treated specimens' tensile properties and fatigue life were also examined and compared. Key findings of this study indicate that complete heat treatment will recrystallize and homogenize the microstructures of specimens printed, regardless of the varying parameters. This transformation shifts the microstructure from a predominantly dendritic structure to an austenitic one, incorporating annealing twins and increasing its hardness correspondingly. This heat treatment schedule produced nearly comparable tensile and fatigue properties, irrespective of the parameter variations. This investigation reveals that samples produced at the lowest laser power (350W) demonstrated a finer microstructure, improving overall mechanical properties. This research provides an efficient post-processing HT schedule for LP-DED Inconel 718 for aerospace applications. It

contributes to the material's characterization and the printing process's standardization.

TABLE OF CONTENTS

LIST OF TABLES

LIST OF FIGURES

CHAPTER 1: INTRODUCTION

Inconel 718 is a Ni-Fe alloy recognized as the most popular Nickel superalloy globally, accounting for 54% of the Nickel-based superalloy market share. Its popularity is due to its excellent thermomechanical properties; this alloy can maintain its mechanical properties at high temperatures up to 650°, making it exceptional at evading creep, fatigue, and corrosion failure. Alloying elements such as Cr, Fe, Nb, Mo, Ti, and Al are added into a Ni gamma matrix to create a precipitation-hardened alloy with a face-centered cubic (FCC) lattice. The main strengthening phases are gamma and gamma prime; the incoherency between these two allows the strain-hardening properties of alloy 718, which is renowned for this. Inconel 718 is extensively used in the aerospace industry to fabricate gas turbines, jet engines, manifolds, rotor shafts, and other components, which can add up to 50% of the weight of an aircraft engine. [1-2]

Traditional manufacturing of Inc 718 has proven especially challenging; mechanical stresses on tools and cutting temperatures rise high. This can result in high manufacturing costs and low productivity. These challenges are solved when manufacturing Inconel 718 with Metal Additive Manufacturing (AM). [1,3] Metal Additive Manufacturing offers several other advantages: the ability to build complex-shaped structures, material optimization, and a short manufacturing cycle.

[3,4] Moreover, the laser or electron beam energy density is high enough to process many materials, including most metals. [4]

Moreover, the laser or electron beam energy density is high enough to process many materials, including most metals. [4]

Understanding the capabilities and constraints associated with each AM process is critical to producing high-quality components. Out of the seven process categories comprised by the international standard ISO/ASTM 52900 [79], directed energy deposition (DED) and laser powder bed fusion (L-PBF) both allow for the fabrication of metal components with near full density, while other process categories remain in development. [80]

L-PBF technology uses a high-power laser to melt and fuse individual layers of metal powder. The feedstock is delivered onto the building platform, where the powder is selectively melted and solidified according to a CAD design. [81] This method is the leading technology in metal AM due to its capability to produce high-resolution and high-quality parts with superior mechanical properties, surface finish, and complex geometries. Minimum feature sizes can reach ~ 0.2–0.4 mm, and maximum part sizes reach 300-400 mm. [13,14,80] Compared to DED, L-PBF feature resolution is finer, and cooling rates are notably higher. [82] Conversely, DED technology stands out for its ability to deliver a feedstock material and an energy source simultaneously to a specific location (melt pool). [27] This technology, used for larger components with lower resolution than those produced by L-PBF, with minimum feature sizes of ~ 1 mm, is a fascinating tool in the aerospace industry. The DED process, with its dimensional freedom, allows for the production of larger components with coarser resolution. What's more, this process is not limited to specific materials, as it can print Inconel, Titanium, stainless steel, and more. [84]

NASA has demonstrated large-scale Laser Powder Direct Energy Deposition applications focusing on rocket engine components such as large-scale wall nozzles and power head components. [39]

LP-DED presents many advantages to the industry, but as with any other manufacturing method, it faces challenges. During manufacturing, internal defects such as balling, porosity, cracks, powder agglomeration, and thermal stresses between printed layers can be developed. Post-processing operations such as heat treatments and machining are required to remove these defects and improve the build's mechanical properties and surface quality. [4, 25,26]

The present study examines and compares Inconel 718 alloy printed with LP-DED varying laser powers (350W, 750W,1070W, 2000W, and 2620W) with the added post-processing HT consisting of stress relief anneal at 1065°C, HIP at 1165°C, solution treatment at 1065°C, and precipitation treatment (double aging) at 760°C and 650°C to observe changes in microstructure and mechanical properties. The mechanical properties investigated in this study were tensile, Vickers hardness, and low cycle fatigue.

1.1.Motivation

To report how different laser powers (350W, 750W, 1070W, 2000W, and 2620W) and heat treatments (SR, HIP, SOL, AGE) affect the microstructures and mechanical properties (fatigue, tensile, and hardness) of LP-DED Inc 718 fabricated samples.

1.2.Thesis Objectives

- To assess the relationship between process parameters and material properties.
- ·To study the effects of the selected heat treatment on the properties and microstructure of Inconel 718.

CHAPTER 2: LITERATURE REVIEW

2.1Different AM Technologies

Additive Manufacturing, often called 3D printing, is a developing manufacturing method that employs layer-by-layer systems using aided computer design to build 3D products with complex shapes and functional properties. Different approaches to AM have been developed, such as techniques like fused deposition modeling (FDM), stereolithography (SLA), selective laser sintering (SLS), powder-blown direct energy deposition (DED), etc. Each of these offers unique advantages and applications, and each method uses different materials and processes to build parts with tailored properties from polymers to ceramics and metals. These can be categorized based on the processes and technologies involved. Various industries have adopted AM due to the range of possibilities it poses. In the aerospace and automotive sectors, it allows the production of lightweight yet durable components, enhancing performance, lowering build times, and optimizing material usage. It enables the customization of medical implants and prosthetics tailored to individual patient needs in healthcare. Fig 1. Shows a schematic of the industrial adoption of additive manufacturing. [5,6,99, 100]

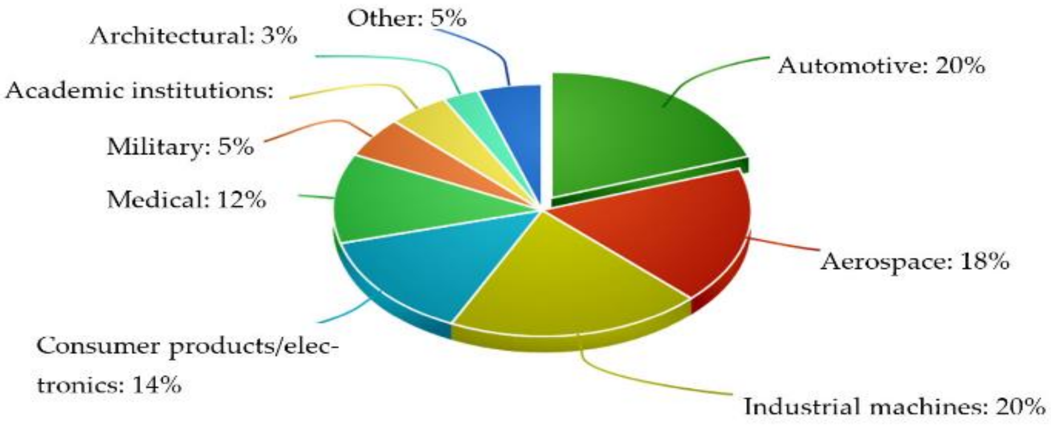

Figure 1. Industrial adoption of additive manufacturing

AM additionally proposes advantages that traditional manufacturing lacks, such as greater design freedom, allowing for creating complex geometries that would otherwise be impossible to manufacture. Furthermore, AM optimizes material usage efficiency compared to traditional manufacturing methods, as it only utilizes the material required to build the part. More advantages of this rising manufacturing method include rapid prototyping and cost reduction. [5,6,99]

Significant advancements in AM have made it a practical choice for mass production. This is evidenced by the increasing number of companies integrating AM into their production processes to meet the ever-evolving market demands. [99]

Fig. 2 shows the varying AM technologies available. These will be briefly described below. [6]

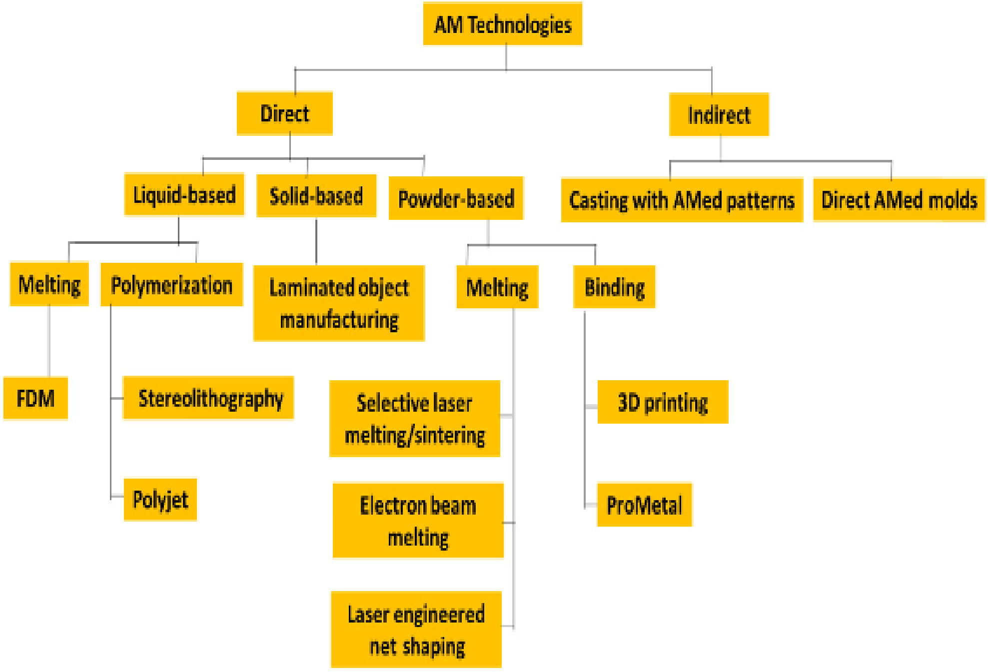

Figure 2. Flow chart of varying AM technologies [5]

2.1.1. Stereolithography

Stereolithography is an AM technique that builds layer by layer using a photosensitive polymer. Building with stereolithography starts with a CAD model, which is converted into a standard tessellation language (STL) file. Further, the STL file is sliced, translating the model from 3D into a 2D model containing the cross-section information.

Each layer will be cured on a build platform by an ultraviolet laser and solidified until the desired structure is obtained (Fig. 3). [6,7,9] The duration of the resin is an exothermic polymerization process characterized by cross-linking reactions. [8] Furthermore, the printed part will undergo a subsequent UV curing cycle to solidify the outermost layer of the part completely.

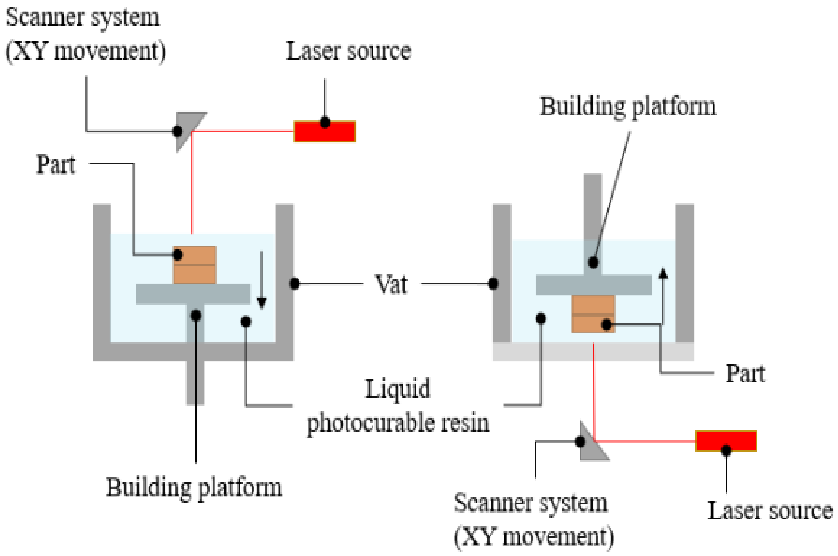

Figure 3. Schematic of stereolithography process [6].

2.1.2. Fused Deposition Modeling (FDM)

Fused Deposition Modeling (FDM) is a layer-by-layer process where a nozzle deposits a semi-liquid thermoplastic filament onto a build plate. This extrusion will be approximately 0.25mm and lower. FDM is mostly used for fast prototyping since it can build large geometries at lower costs without requiring chemical post-processing. The most used materials in FDM are polycarbonate (PC), acrylonitrile butadiene styrene (ABS), wax metals, and ceramics. However, FDM structures can have lower resolution than other AM methods due to poor layer thickness control. [5,6,8,9]

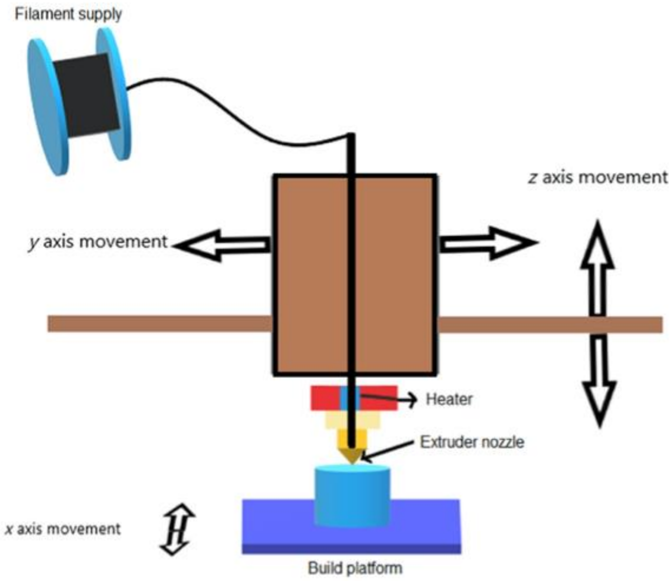

Figure 4. Schematic of FDM process [9].

2.1.3 Polyjet

The Polyjet technology combines the inkjet technique and photopolymerization process to manufacture 3D models. An inkjet head moves in the x and y directions, depositing droplets of photopolymer, which are later cured and solidified by ultraviolet lamps. The process will be repeated after printing a thin material layer until the model is completely formed. Polyjet models have good resolution; the layer thickness achieved is 16um or lower. Post-processing is required since structures are built with supports or overhangs. However, these structures can be weaker than others produced by stereolithography or selective laser sintering. [5,6,11,12]

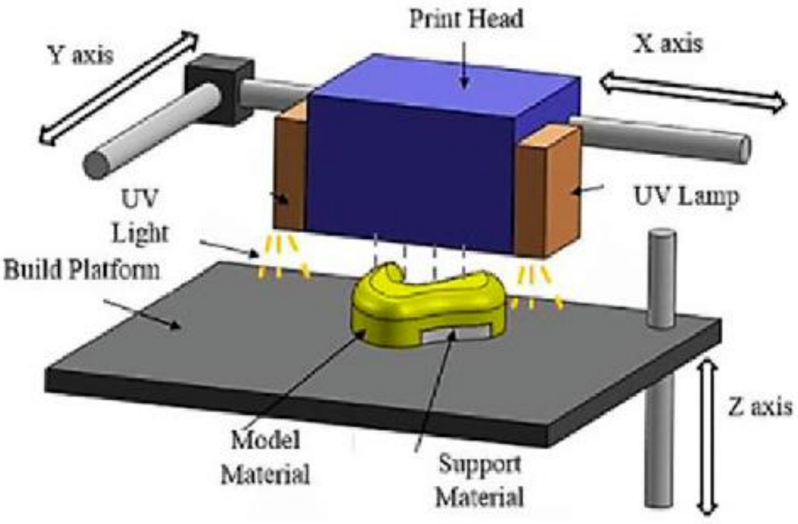

Figure 5. Schematic of polyjet process [6].

2.1.4 Laminated Object Manufacturing (LOM)

Laminated Object manufacturing (LOM) is a solid-based approach that combines additive and subtractive techniques to create a part layer by layer. LOM employs material in sheets; each sheet will be coated in an adhesive before bonding to another sheet. This lamination will be consecutive until the build finishes. Further, a carbon dioxide laser will be used to cut the material to its desired shape, and the depth of each cut must be the same as the layer thickness during lamination to avoid destroying previous layers. LOM is a versatile technique as it can be built with various materials such as composites, metallic materials, paper, plastics, fabrics, and synthetic materials. Moreover, this technique is cost-effective, reduces internal stresses, and prevents changes to the material's properties. However, as with any other AM technique, it has downturns, including poor z-axis accuracy and material waste. [5,6]

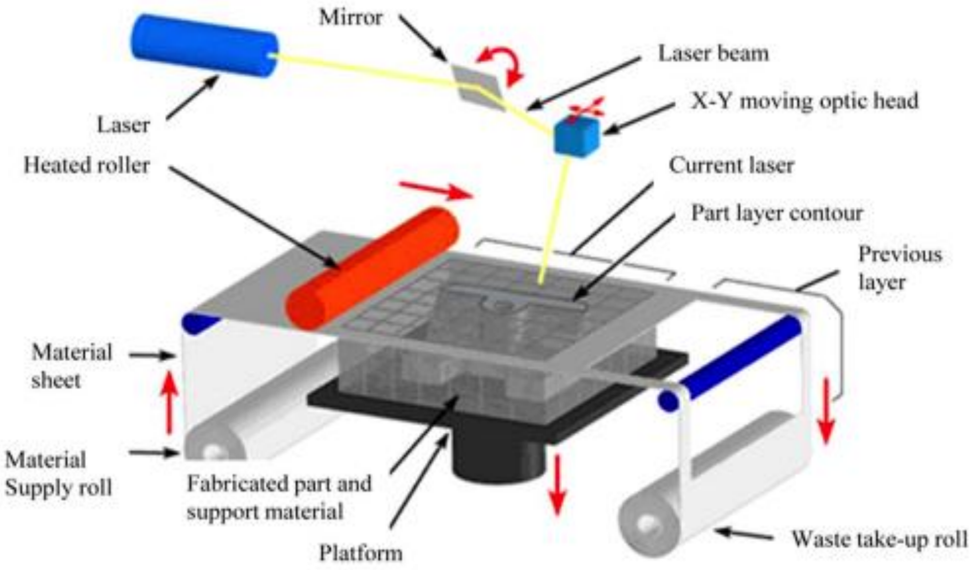

Figure 6. Schematic of LOM process [5].

2.1.5 Laser Powder Bed Fusion (L-PBF)/Selective Laser Melting (SLM)

Laser powder bed fusion (L-PBF), as we know, was first created with the name selective laser melting (SLM) by Carl Deckard from the University of Texas at Austin in 1987. More commonly known today as L-PBF, it has been the leading candidate for fabricating critical components in industry due to its ability to produce near-net-shape parts with superior mechanical properties, surface finish, and complex geometries. This process is adequate for building multifaceted parts with densities as high as 99.9% via a high-power-density laser. [13,14] SLM/L-PBF systems consist of three major components: (i) laser and scanning system, (ii) controller system, and (iii) build chamber (Fig. 7).

The printing process is initiated by applying a thin layer of powder onto the build platform. A high-energy laser beam melts the metallic powder, rapidly solidifying it into a layer. This process repeats until the part is fully printed.

Parameters shall be selected based on machine specification, types of materials, and interaction with each other. Understanding the effects of each parameter is essential for build optimization, given that the final products' mechanical properties depend on process parameters. Energy density and scan strategy are optimal parameters that minimize internal defects that can cause poor mechanical properties if misconfigured. Further, most printed parts need post-processing to improve surface roughness and remove internal defects such as porosity, cracks, thermal stresses, and powder agglomeration that appear between printing layers. [4]

L-PBF uses metal powders as feedstock materials. These can include metals and alloys such as nickel-based alloys, stainless steel, aluminum, titanium, copper, etc. It is recommended to use a powder feedstock with a diameter size range between 15-45µm and a predominant spherical morphology exhibiting a uniform size distribution. Particle shape has been shown to significantly affect flow, discharge rates, and clogging in hopper systems.

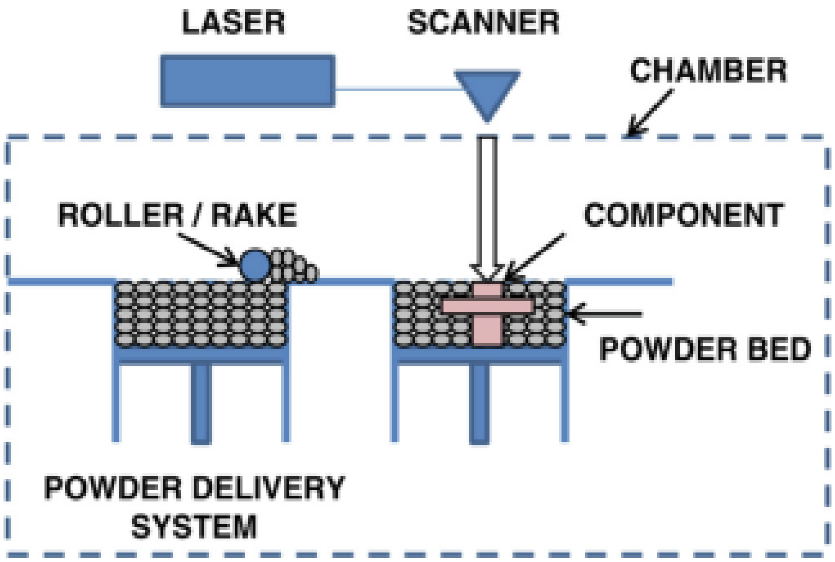

Figure 7. Laser powder bed fusion build chamber [11].

2.1.6 Electron Beam Melting

Electron beam melting (EBM) is a process comparable to SLM as both are a layer-by-layer powder bed fusion technology. These systems form a powder bed by raking powder fed from cassettes or hoppers into a thin layer, which is then melted selectively by a laser or electron beam respectively and solidified in an inert environment. [16] Some differences are the beam type: SLM employs a laser beam, EBM an electron beam with a voltage range 30-60kV. The powder bed is also kept at a higher temperature (>870K) in EBM. Further, this system involves more process parameters than SLM, such as beam diameter, beam power, beam scanning velocity, beam focus, beam line spacing, scan strategy, and contour strategies. Thus, parameter optimization is more challenging. [4,17]

Fig. 8 illustrates the build chamber (a), where the powder is preheated by the focused electron beam with a voltage of approximately 30mA to 0.8Tm (melting temperature) and scanned. Following, the powder is released from the hoppers and raked onto the build platform, which is lowered with each layer until the component is finished (b). [16,18]

EMB can be potentially more expensive and time-consuming; however, oxidation and porosity are generally prevented because of its vacuum atmosphere. EBM can also process brittle materials due to slower cooling rates.

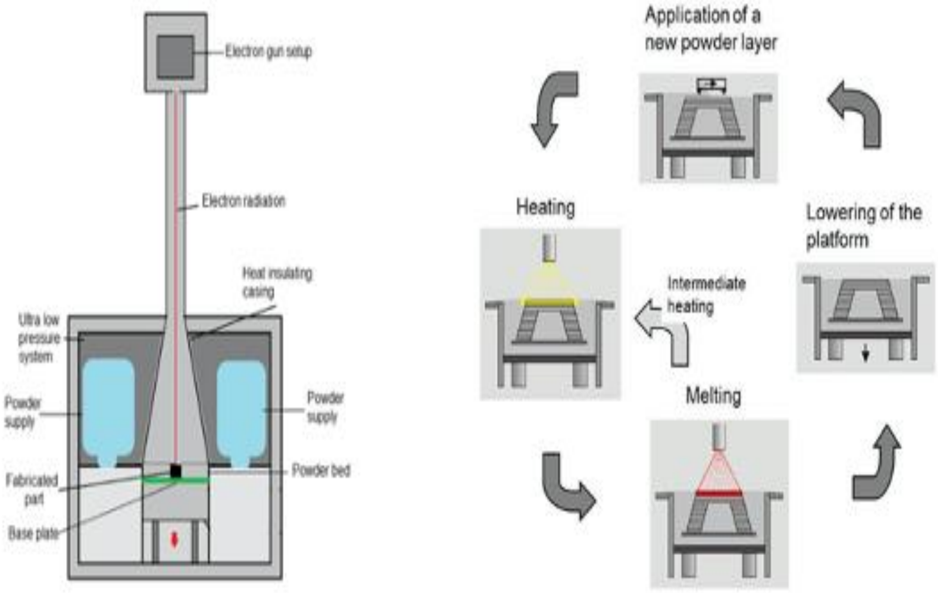

Figure 8. EBM a) build chamber b) build process [16.18].

2.1.7 Binder Jetting

Binder Jetting is a non-fusion additive manufacturing technology where a shape is formed and solidified only after post-processing. Fig. 9 shows the different components of a binder jetting system, including a powder supply platform, build platform, leveling roller, and binder printhead. A layer of metallic/ceramic powder will be spread by the roller over the build platform, where a liquid binder is selectively deposited to adhere to the loose particles in that layer. Like other AM techniques, the build platform will be lower by the distance equal to the thickness layer of the part. This process will be repeated until the “green part" is finished and post-processed. After the build is completed, it will be submitted for post-processing, which may include curing, de-powdering, sintering, infiltrations, annealing, and finishing. Although binder jetting is a cost-effective and versatile AM method, post-processing can be costly. However, as BJ does not involve heating, no residual stresses are created as in parts built with other techniques.

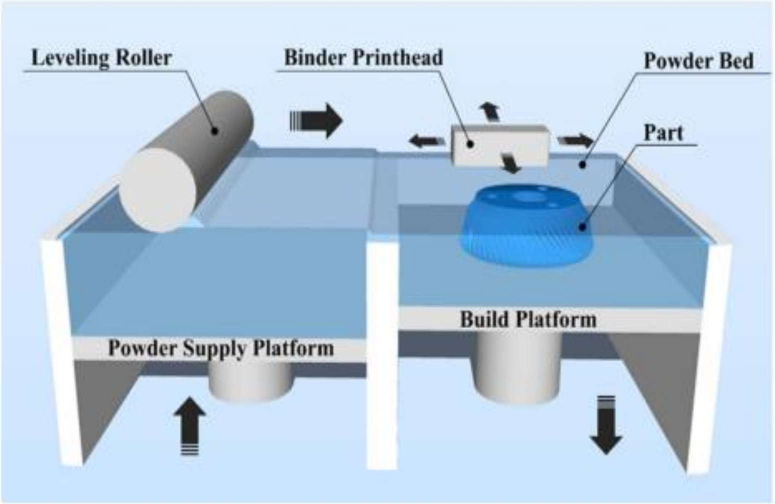

Figure 9. Schematic of BJ system [5]

2.2 Laser Power Directed Energy Deposition (DED): LP-DED History, LP-DED Process Characteristics, LP-DED Workflow and Machine Operation Review

2.2.1 History/Timeline

Directed energy deposition (DED), also known as laser-engineered net shaping (LENS), originated in the "Welding AM" circa the 1980s, using various welding and thermal spray technologies. [26,27] In his 1984 patent [26], Harter described this process as “a manner of producing a metal article by depositing metal by the arc process in successful intersecting fusion beads along a non-adherent base… until the desired thickness dimension is attained”.

Directed Light Fabrication (DLF) was introduced in 1995 by Los Alamos National Laboratory as a computer-aided technology with the capacity to produce an entirely deposited planar metal layer of approximately 0.1mm in thickness successionally until the completion of a 3D part as depicted in Fig. 10. The main components of DLF were specified as a Nd:YAG laser, a metal powder delivery system, and a beam positioner. Furthermore, the principal parameters were listed as laser power, velocity between the laser focal spot, layer thickness, and powder mass flow rate. [28]

In the late 1990s, Laser Engineered Net Shaping (LENS) was invented by Dr. Donald Godfrey and his team at Sandia National Labs, influenced by laser cladding. [27] The LENS process is the most common means to achieve powder-based DED today. [29]

Throughout the 2000s, advancements in laser technology and materials science allowed companies like Optomec to commercialize DED/LENS technology, expanding into the aerospace, automotive, and medical industries. In 2017, standardization efforts by ASTM International further solidified the terminology and recognition of DED. [21]

Different commercially available technologies, categorized by their energy source and the type of feedstock they use, include directed light fabrication (DLF), direct metal deposition (DMD), laser metal deposition (LMD), laser solid forming (LSF), electron beam additive manufacturing (EBAM!), LENS, and wire plus arc additive manufacturing (WAAM). [21] Some DED systems are capable of depositing multiple materials simultaneously and can deposit material across various axes to produce reasonably complex geometries. DED is also used to repair pre-existing parts. [21]

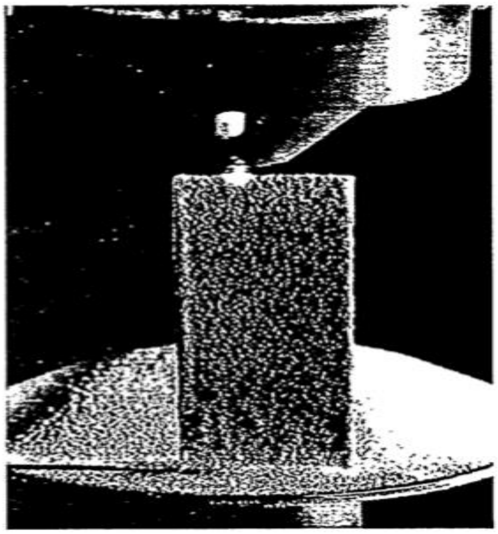

Figure 10. Depiction of 3D 316 SS part by LANL [26].

2.2.2 Laser and Feedstock Delivery; Powder vs Wire

DED allows the delivery of a feedstock material and an energy source simultaneously at a given location. The laser and its power capabilities vary among DED machines. Most systems utilize an ND:YAG (neodymium-doped yttrium aluminum garnet) laser with a typical power raging between 1 and 5kW. Nevertheless, any laser with sufficient power to melt the material, including carbon dioxide and pulsed-waved lasers, is acceptable. [27]

DED processes can utilize a powder (LP-DED) or a wire feedstock (HRW-DED) [33,35] (Fig. 11). A powder DED powder feeding subsystem includes a powder feeder, powder nozzle, and tubing connecting these components. It also includes a laser subsystem consisting primarily of a high-power laser source, a zoom optic device, and optic fibers. Additionally, inert gas sources will be present along with process monitoring and control devices, compressed air sources, a cooling device, etc. Moreover, this process is accomplished by simultaneously increasing mass input and energy input by optimizing laser power and augmenting powder feeding rates. HP-DED will require a high-power laser source and an innovative nozzle for continuous powder delivery. [34] Alternatively, HRW-DED continuously feeds metal wire into a melt pool at a specific speed (usually 0.5-5m/min). The wire is subsequently melted and solidified. Wire DED is known for material utilization optimization, high-energy utilization optimization, and the absence of powder pollution. However, energy input insufficiency can lead to defects such as un-melted wire in builds. Thus, the build quality allowed by wire feeding depends on energy density and wire feeding rate. Low heat input and a higher process speed result in difficulty in fully melting the filler wire. [34]

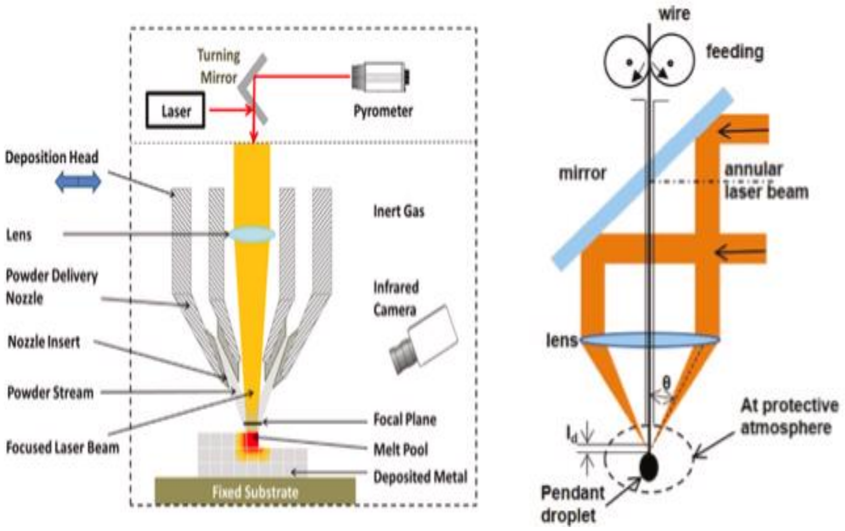

Figure 11. Schematics of Powder and Wire laser deposition [27,34].

One drawback of powder deposition is that, despite its widespread use as a feedstock for metals and ceramics, not all powder is effectively captured in the melt pool, resulting in excess powder utilization. In contrast, wire deposition boasts a high deposition rate, ensuring that the volume of the deposit closely matches the volume of the wire fed. However, this can lead to near shape builds with compromised dimensional accuracy and surface finish. [35]

2.2.3 Feedstock Materials

Feedstock materials are limited for wire deposition DED compared to powder-blown DED; hence, powder is the most common feedstock in the DED industry. Most commonly, this powder is administered via pneumatic powder metering. Powder particle size will be significantly larger in DED than in PBF, ranging between 50-150um and 10-50um. Larger particle size powders are preferred in DED, as well as a spherical powder shape due to increased flowability; additionally, larger particles will most likely break the surface tension of the melt pool upon impact, thus increasing catchment efficiency. However, substantial powder particles will lead to higher surface roughness. [35-37]

Defects related to porosity in DED builds can be attributed to the quality of the powder feedstock and, unfortunately, can't be improved by any post-processing as a build parameter or alloy design-related defect could. Lower fatigue strength and fracture toughness caused by voids in the build must be avoided by including high-quality feedstocks that target successful properties in a built component. [37]

2.2.4 LP-DED Workflow

Fig. 14 shows a schematic of a typical workflow for the LP-DED process [39]:

1. File preparation: Prepare a CAD model using the “rules of thumb.” The designated computer-aided design (CAD) 3D model will be exported as a Standard Tessellation Language (STL) file and sliced into horizontal layers representing each cross-section of the final build. These files will include “rules of thumb” regarding overhangs and support structures, orientation, material considerations, layer thickness, part size, tolerances, etc.[39,40,42]

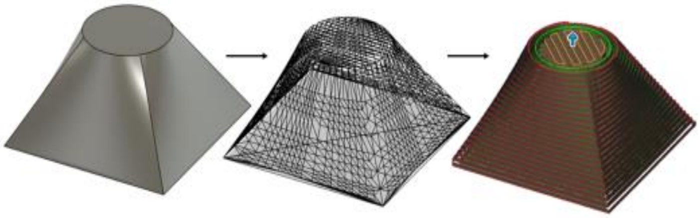

Figure 12. CAD model, mesh representation, and sliced sequence of toolpath vectors. [39]

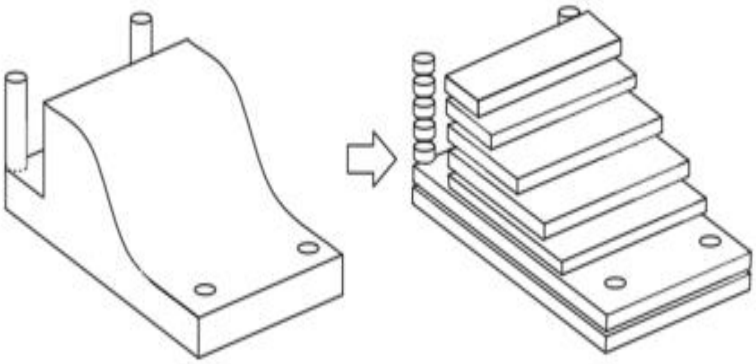

Figure 13. Example of "sliced" model in layers. [39]

2. Toolpath generation: After having the 3D CAD model sliced into horizontal layers, a toolpath must be generated based on the sliced layers. This toolpath will determine the movement of the laser during the printing process and trace the outline of the area rastering the laser back and forth in a serpentine

pattern. Strategies like contouring and infill are employed as well as considerations such as supports, and processing needs are integrated. [39,40,42]

3. Machine preparation: Machine setup involves cleaning, installing, aligning, loading metal powder, and leveling the build plate or substrate. This could be a plate or a component being added or repaired.

   Before starting the DED build, thorough machine preparation is important to ensure ideal printing conditions. First, the build platform must be clean and aligned to guarantee precise material deposition. Next, the nozzle must be checked and calibrated. Moreover, it is important to ensure the chamber is purged of impurities, verify the material feed system is working well, etc. [39,41,46]
4. Additive manufacturing process/DED build of part: The powder will be dispensed into a carrier gas stream, which will transport it through tubes to the printing nozzle, and the laser will be activated to deposit a melt pool onto the build plate layer by layer from bottom to top according to the pre-determined toolpath until the final part is completed. [40,46]
5. General Powder Removal: Refers to removing excess powder from the build that didn't fully melt. After completing the DED process, powder removal is required to extract the printed part from the surrounding powder in

preparation for post-processing. Commonly, de-powdering is done with wire brushes or vacuums. [39,42]

6. Stress relief: Stress relief minimizes residual stresses and internal distortions formed during the printing process. Because of its unique thermal cycles, DED builds often require stress relieving to remove residual stresses caused by thermal gradients. This can be achieved by a post-annealing heat treatment of 70% after de-powdering and removal. After heat treatment, the part is gradually cooled to avoid the formation of new stresses. Stress relieving improves the mechanical properties of the build, improves dimensional stability, and reduces the risk of distortion or cracking during machining or in service. [43-45]
7. Build plate removal: After de-powdering the build plate must be carefully extracted from the machine. [39]
8. Post processing operations: During manufacturing, internal defects such as balling, porosity, cracks, powder agglomeration, and thermal stresses between printed layers can be developed. Post-processingPost-processing operations such as heat treatments, machining, cleaning, polishing, welding, and brazing are required to remove these defects and improve the build's mechanical properties and surface quality. [4, 39, 46]

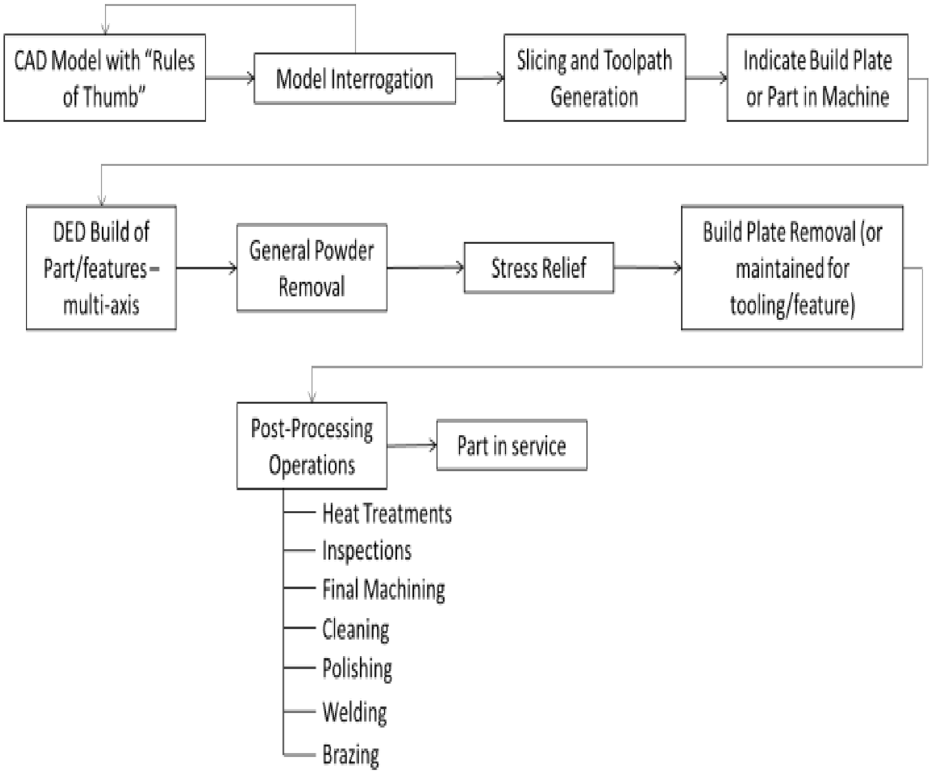

Figure 14. DED typical workflow

2.3LP-DED Fabrication of Inconel 718: Feedstock and Build Characterization

2.3.1 Chemical Composition and Feedstock Properties

Inconel 718 is a hardenable nickel-chrome-iron-molybdenum alloy (Table 1 shows the chemical composition per AMS 5596). Hardening is possible by adding alloying elements such as niobium, titanium, and aluminum and induced by heat treatment in the temperature range of 593 to 816°C. [51] It is extensively used in the aerospace industry, steam generators, nuclear power plants, and the defense department due to its outstanding mechanical properties, creep resistance, fatigue endurance, and corrosion resistance. [52]

Alloy 718 is available for AM in rod, bar, wire, forging stock, plate, sheet, strip, and powder. Powder is typically fabricated by gas atomization, where molten metal is atomized into fine droplets using a high-pressure gas stream. These droplets solidify into powder particles upon contact with a substrate or metal plate. [53]

Spherical powder particles are preferred for feedstock powders to increase flowability. [37] Moreover, a particle size from 50-150um will also allow for easy flowability and higher catchment efficiency; this is larger than the particle size used for SLM. [35] Fig. 15 a) and b) show a cross-section and a scattered electron microscope (SEM) image of Inc 718 powder particles with evident gas entrapment and satellite formations. [52] Gas porosity entrapment in powder can compromise the quality of the final printed product as it can lead to poor mechanical properties and lower density. It has been discussed [37], and the best way to lessen these features is to control the entrapment in the original powder-making process.

Table 1. AMS Inc 718 chemistry spec

* maximum content

Alloy 718 Component	Element wt.%											
	Ni	**Cr**	**Fe**	**Nb**	**Mo**	**Ti**	**Al**	**Co**	**C**	**Mn**	**Si**	**P**	**S**
AMS 5596 A Standard Wt%	50-55	17-21	Bal	4.75-5.50	2.80-3.30	0.65-1.15	0.20-0.80	1.0*	0.08*	0.035*	0.035*	0.015*	0.015*

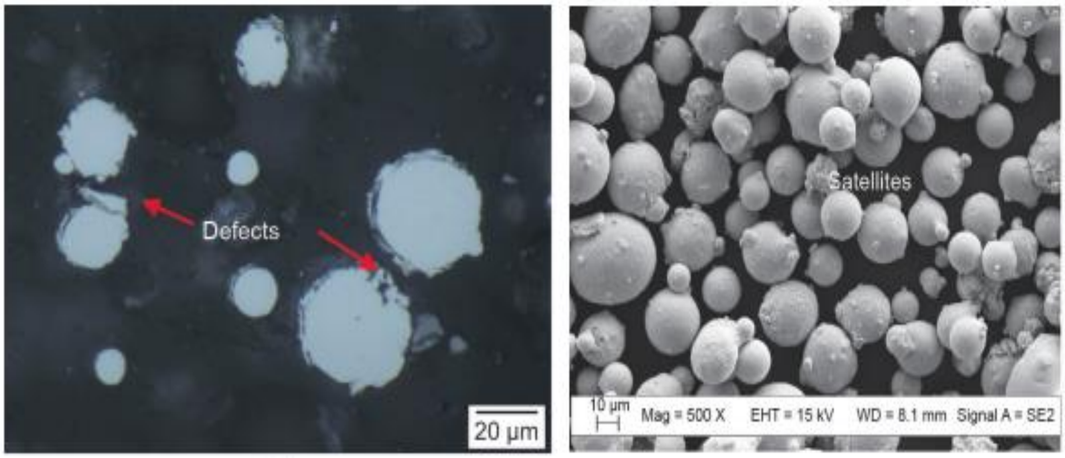

Figure 15. Micrograph and SEM image of Inc 718 powder particles with satellites [52].

2.3.2 Microstructure: LP-DED

It is hard to predict the microstructure of DED printed Inconel 718 with certainty due to the complicated thermal cycling it undergoes during printing (exemplified in Fig. 16): the deposited material experiences remelting, re-solidification, and solid-state phase transformation depending on factors such as heating rates, cooling rates that can reach up to 10^3-10^5K/s, thermal gradients, number of thermal cycles, etc. [47] Some process parameters that affect the thermal history of the material are powder feed rate, laser power, and laser scanning strategy. [49]

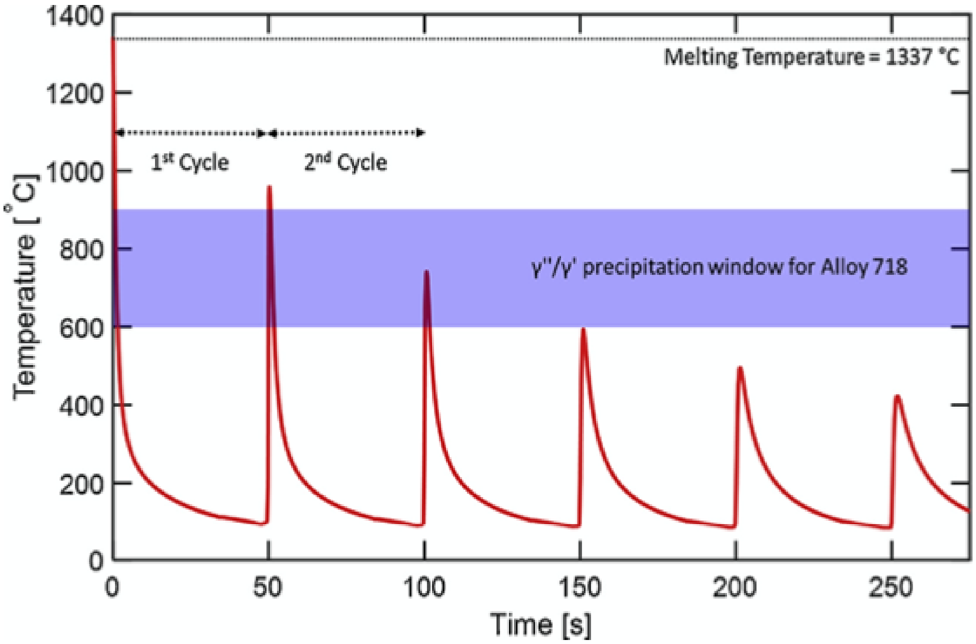

Figure 16. Time-temperature history measured at 1st deposited layer [47].

It has been observed [49] that a higher traverse velocity and lower laser power result in a finer microstructure due to higher cooling rates. Conversely, lower cooling rates resulting from slower traverse speeds and higher laser powers will yield coarser microstructures.

Bontha et al. [54] established the relationship between dendrite morphology, temperature gradient (G), and solidification velocity (R) during the DED process. This allows for predicting the microstructure between a columnar, equiaxed, or mixed morphology. [31]

The typical as-built microstructure of a 718 printed sample consists of columnar dendrites, which usually grow in the <1 0 0> orientation parallel to the deposition, as depicted in Figure 16. The columnar morphology extends through the deposited layers due to the re-melting of previous layers and heterogeneous nucleation of γ dendrites.

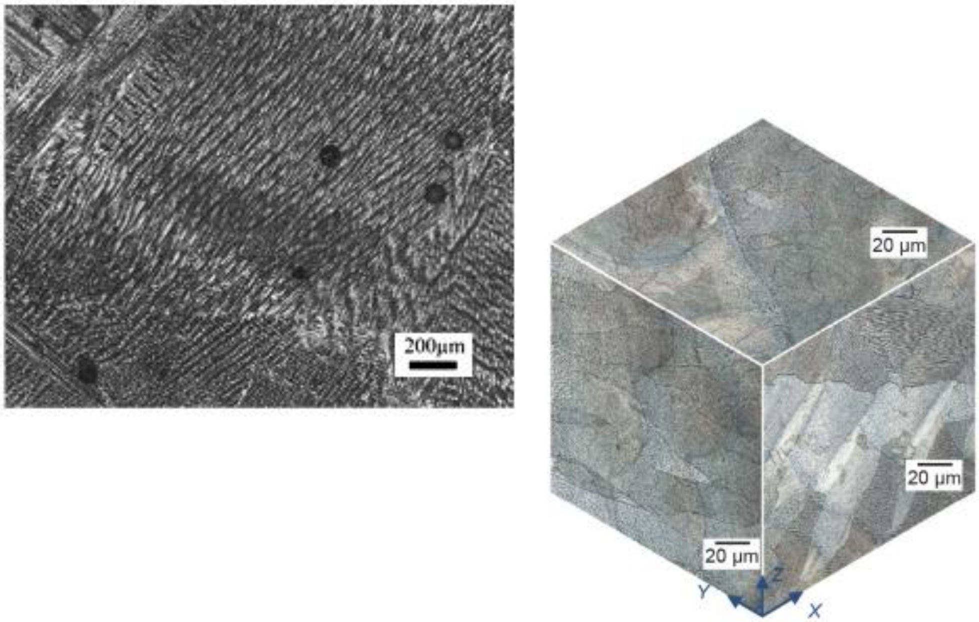

Figure 17. Typical as deposited microstructure of DED Inc 718 showing a dendritic columnar morphology [50].

Moreover, it has been shown [47] that upon solidification, alloying elements molybdenum (Mo), niobium (Nb), and titanium (Ti) segregate into interdendritic regions. This micro-segregation is evident in the Nb and Mo-rich and Laves phases. Post-heat treatment processes are required to eliminate these brittle phases (Laves phase, δ) and reduce residual thermal stresses. Heat treatment will also improve the microstructures of deposited builds, which will positively influence their mechanical and physical properties. [2]

2.3.3 Microstructure: LP-DED HT

LP-DED Inconel 718 in the as built condition contains the brittle Laves and δ phase which will form because of micro-segregation of Nb and Ti mostly into the inter-dendritic zones [2]. NbC and Laves phase are a product of eutectic reactions when the concentration of Nb, Mo and C in the melt is too high [56]. Such phases can negatively impact the mechanical properties of alloy 718. Post processing heat treatment is needed to dissolve the Laves and δ phases, uniformly distribute alloying elements Ti al and Nb through the matrix and precipitate γ’ and γ’’ to reach peak strength. [2]

Standard AMS 5662 indicates standard heat treatments for Inc 718 as a solution treatment followed by a two-step or double aging (see Table 2). Solution treatment intends to dissolve the leaves phase and additional precipitates that form during fabrication. Double aging is performed to produce strengthening γ’ (Ni3 Nb) and γ’’ (Ni3 (Ti, Al)) phases. [57]

Table 2. AMS spec heat treatment for Inc 718

Spec **AMS 5662 [58]**	**Temp(°C)**	**Time**	**Cooling**
Solution Treatment	954°C	"time commensurate with thickness"	AC or faster
1.Precipitation Treatment (aging)	718-746°C	8 hr	Furnace cool to 649°C
2. Double Aging	649°C	Hold for total time of 18 hr	AC

Moreover, this section will discuss stress relieving, homogenizing (HIP), solutionizing, aging, and quenching to understand further the effects of ST-age heat treatments on the microstructure and properties of DED Inconel 718.

2.3.3.1 Stress Relieving

The objective of solution annealing or stress relieving is to provide an equilibrium state for the processed material by removing residual stresses and minimizing microstructural defects such as internal distortions. [60] The part is heated to a specific temperature below the material's melting temperature but high enough to induce relaxation of internal stresses accumulated during the printing process. After the heat treatment, the part is gradually cooled to avoid the formation of new stresses. Stress relieving also aims to homogenize the microstructure for optimal microstructure and mechanical properties. [61] ASTM F3055 indicates the stress relieving process for Inc 718 at 1065 °C ±15 °C (above the γ', γ'' and δ solves temps) for 90 min −5/ + 15 min. [62]

2.3.3.2 Hot Isostatic Pressing (HIP)

HIP-ing is an important post processing technique used in AM to enhance material properties and structural integrity of builds. HIP serves as a post processing method that applies a heated gas under an elevated pressure up to 10,342 to 206k MPa to densify metal parts to nearly 100% theoretical density by diffusion bonding closing of the pores. This process is carried out in an inert gas environment, typically argon. The combination of heat and pressure helps to eliminate internal voids, porosity, and microcracks present in the printed parts, resulting from the rapid heating and cooling cycles of some AM processes. HIP-ing also increases ductility and extends fatigue life. [29]

ASTM indicates a HIP process for Inc 718 in the range of 1120-1185°C for 4 hours with an applied pressure of 100 MPa [62]. This duration assures the dissolution of γ’, γ’’, δ, and laves phase as well as the homogenization of the material.

2.3.3.3. Solutionizing

Solutionizing is a post processing heat treatment aimed to dissolve any secondary phases or unwanted precipitates that may have formed during the printing process. A most common solution heat treatment for Inconel 718 proved effective in industry is any in the range of 941°C-1010°C for an hour per 25 mm in thickness. These temperatures are above the solvus temperatures of both γ’and γ’’ but below δ. Which acts as a grain boundary pinner preventing grain growth. The part is held at this temperature for enough time to allow for the dissolution of such precipitates and for the diffusion of solute atoms throughout the matrix.
After holding at the solution temperature hold, the parts must be quenched to “freeze” the microstructure in its homogeneous state. [101,102]

2.3.3.4. Double Aging

Double aging is a heat treatment aimed towards increasing the strength, creep, and resistance of Inc 718. The first aging step consists in heating the part to a temperature below the solvus line, allowing for the precipitation of fine, coherent, precipitates such as γ’ and γ’’. Aging is crucial in recovering the initial strength of the material by creating precipitates within the matrix which will prevent dislocation slip hence improving such [60].

Following the first aging step, the parts are cooled to RT and subjected to a second aging step which consists of holding the parts at a lower temperature for a longer duration. This step allows for further precipitation and growth of strengthening phases.

Double aging is most used for AM Inconel 718 intended for high temperature applications in aerospace, gas turbine engines because of its enhanced mechanical properties and reliability in service. [101, 102]

2.3.3.5. Quenching

Quenching is recommended after solution treatment to avoid grain growth that would result for larger cooling rates.

The purpose of the solution-age heat treatment is to eliminate scan strategy effects by recrystallization and grain growth which eliminate the anisotropic columnar morphology of the as built parts. [102]

2.3.4 LP-DED Build Defects

In addition to the multiple advantages and versatile capabilities inherent to the DED process, like any manufacturing method, it also has its limitations. Some of these limitations include shrinkage and residual stresses due to local thermal gradients, lower dimensional resolution, higher surface roughness, porosity, keyholing, laser spattering, balling, cracking, and de-lamination. [21] Some of these defects will be discussed in more detail below.

2.3.4.1 Residual stresses and distortions

Residual stresses and distortions can develop during the deposition and cooling processes due to high cooling rates and important thermal gradients. These can cause induced phase transformations and consequently cracking, delamination, degradation of fatigue life and premature failure. To mitigate these effects, the substrate and the chamber can be preheated to reduce thermal gradients. The printed part can also be subjected to post processing methods including heat treatments. [21]

2.3.4.2 Porosity

LP-DED produced specimens can exhibit porosity due to too high energy density applied or conversely insufficient energy input (LoF), pre-existing feedstock porosity also influences the total porosity of a finished build, as well as selective evaporation, and gas entrapment. Each has a distinct shape size and formation mechanism.

The process window, as depicted in Fig. 18 represents the range where laser power and scan speed leads to the creation of a stable melt pool. In this window, laser energy is efficiently absorbed by the powder, this allows for the formation of a melt pool that reaches an appropriate depth for strong fusion with the layer beneath, while minimizing excessive re-melting. Variations in laser temperature, and/or scan speed whether exceeding the optimal range or falling below it, can lead to lack of fusion, keyholing, and balling. [21,92]

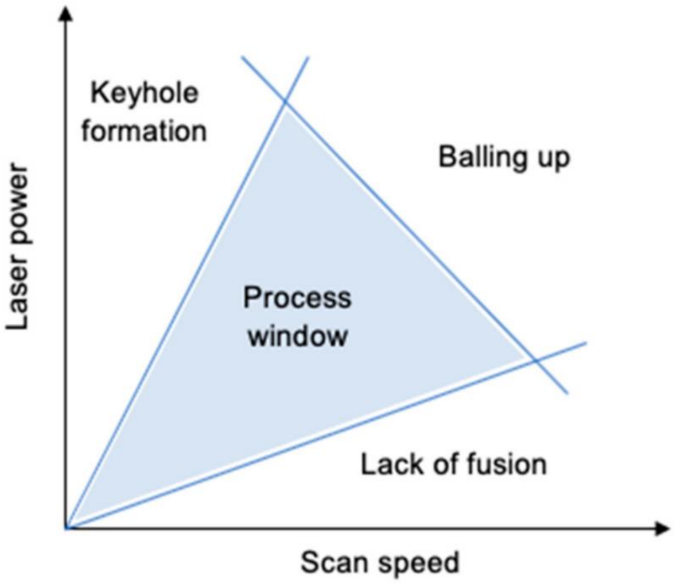

Figure 18. Laser power vs scan speed graph

Lack of fusion is described as a discontinuity between the substrate and the deposition metal or the adjacent layers to fully melt. [103] As observable in Fig. 18, lack of fusion occurs when there is insufficient energy and a high scan speed which results in low bead wettability [104] and an irregular shape discontinuity. [105]

Moreover, as seen in the laser power vs scan speed (Fig. 18) keyhole formation or keyholing occurs when there is an excessive energy input during the melting process. Excessive beam power causes excessive penetration of the metal powder which leaves a pore at the bottom of the melt pool. Keyhole porosity is usually circular horizontally and elongated in the vertical direction. [106]

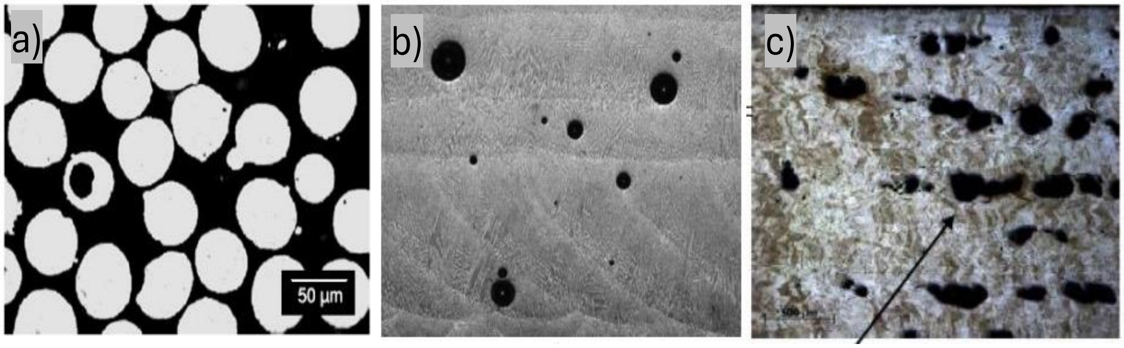

Figure 19. a) Entrapped gas porosity in powder feedstock b) entrapped gas porosity in as built condition, c) lack of fusion

2.3.4.3 High surface roughness

High surface roughness is common in powder blown L-DED and can be consequent to multiple factors including low heat input, large powder particles, and high laser scanning speeds. High surface roughness can be detrimental to the mechanical properties of a build and have adverse effects on dimensions and geometric tolerances. An increase of heat input can be applied to reduce the surface roughness. Reducing the layer thickness in the build and using finer powder particles has also been proved efficient at reducing surface roughness. After the build has been completed post processing schedules and heat treatment will also yield better surface roughness. [21,93]

2.4 Mechanical Properties: LP-DED Inconel 718/HT

Inconel 718 accounts for good mechanical properties such as good strength, good weldability, creep resistance, and fatigue resistance at elevated temperatures. These properties can be attributed to a high amount of strengthening carbides and intermetallic phases. Intermetallic phases γ’ and γ’’ are the most important strengthening components in the alloy as they are coherent to the γ matrix and of “sluggish” nature. However, niobium segregation is not uncommon in this alloy be it in wrought products or in the as built condition of additive manufactured parts. This segregation is undesirable as it will lead to scatter in the mechanical properties caused by macro-segregation, laves phase, and other unwanted carbides. [50]

Tensile properties and hardness are often studied because valuable information these reveal. Yield stress indicates the elastic region of a material or the highest load it can withstand before plastic deformation, and ultimate tensile strength is the highest load the material can withstand before failure. These properties are important considerations for design and applications of a component.

It is important to note that it is not common for additively manufactured Inconel 718 to be put in service in the as built condition as the main hardening mechanism is achieved by post processing heat treatments. UTS and %Elongation in the as built condition are lower and higher respectively which means lower strength and higher ductility, this can be credited to the absence of hardening precipitates γ’ and γ’’. [73] Porosity is also a factor that can negatively affect the mechanical properties of an AM part given that AM processes yield varied levels of porosity depending on the building parameters [74].

Table 3 contains mechanical properties of LP-DED as built, wrought, cast and HT Inconel 718 obtained from literature for comparison. [74-76] Table 3 demonstrates casted Inconel 718 having the lowest tensile properties overall, followed by LP-DED in the as built condition which had lower UTS and YS than wrought and HT but higher ductility on account of the faster cooling rated provided by LP-DED processing. It is also shown how heat-treated Inconel 718 when subjected to HIP, SOL, and aging treatment can achieve high strength comparable to that of the wrought material.

Table 3. Mechanical properties of Inc 718 from literature

	As-built[75,76]	**HIP+SOL+Aged**	**Wrought**	**Cast**
UTS (MPa)	904-1150	1371-1387	1100-1400	780-1060
YS (Mpa)	572, 907	1084-1160	1035-1160	488-900
%El	19-26	10-22	12-21	5-11

As proved from literature, as built LP-DED Inconel 718 must undergo a series of HT to strengthen its ductile characteristics. Post processing heat treatment is of utmost importance not only because of precipitation hardening but also because it can reduce residual stresses up to 20%. [73]

2.4.1 Fatigue Life

Fatigue is a progressive form of fracture resulting from repeated or cyclic loading that can cause the initiation and propagation of a crack. The fatigue life of a component is determined by the number of stress cycles it can complete before failure. Ideally, an in-service part will perform in stresses below the material’s yield strength however, fatigue failure can still happen. [65] Further, some factors that affect the fatigue life of a component are such as environment, stress concentrators, microstructure, and surface finishing. Fatigue can lead to catastrophic failures because of its unnoticeable features.

Fatigue traditionally occurs in three stages: crack initiation, crack propagation, and final fracture. [65,66] Cracks typically nucleate from transgranular slip bands near or at the surface of specimens and can grow up to 50µ before propagating through 60-70% of the material's cross-sectional area to the final fracture. [68] Typical features of fatigue are beach marks and rough surfaces accompanied by shear lip.

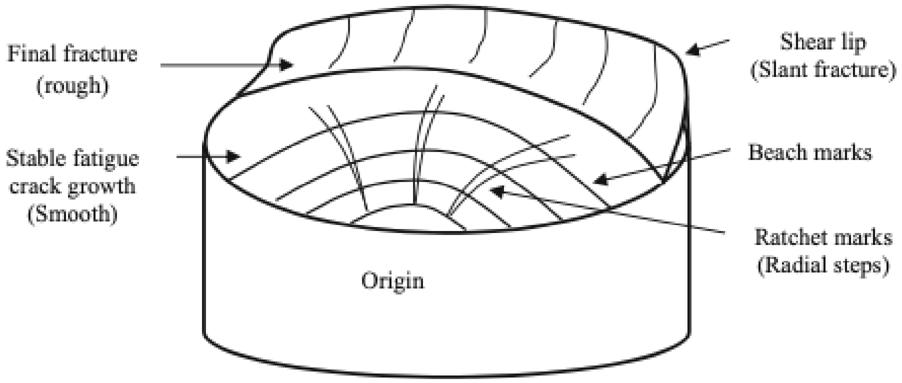

Figure 20. Typical characteristics (macroscopic) of fatigue fracture [65].

As mentioned before, cracks can nucleate or initiate from surface defects or internal pores. Hence, additively manufactured parts tend to have lower fatigue lives than wrought or occasionally cast components, for cracks tend to nucleate in stress concentrators yielded by defects produced during AM processing such as porosity, microcracks, lack of fusion, etc. [2,67]

Johnson et al., explained [68] that fatigue life of AM Inc 718 is shorter than that of wrought components due to the origination of cracks from pores or inclusions.

Where, after initiation cracks propagated in a transgranular mode and final fracture happened in a ductile manner. Moreover, Kelley [69] demonstrated that HZ, HT and machined AM Inconel 718 can achieve similar fatigue properties to those of wrought Inconel 718. Furthermore, it was also demonstrated that pores were not the main stress concentrator for crack propagation, but surface defects were the main reason for inferior fatigue life of AM Inc 718 components. Correspondingly, surface machining for improved surface roughness enhances the component's fatigue endurance. [69,70]

Fatigue life can also be dependent on the microstructure of the processed alloy, recrystallization of a dendritic morphology into equiaxed grains with annealing twins can be detrimental to fatigue life because of the formation of cracks at twin boundaries in HZ samples. [71,72]

CHAPTER 3: EXPERIMENTAL METHODS

3.1Laser Power Directed Energy Deposition

Three types of specimens were built: 126 samples printed with laser power-directed energy deposition (L-PDED) were received, including round tensile rods, tensile and mechanical blocks, and square mechanical rods. Yet only specimens 002-031 were tested. All samples were printed with virgin powder, and each group was printed with different laser powers: 350W, 750W, 1070W, 2000W, and 2620W, and other travel speeds accordingly to observe changes in microstructure and mechanical properties throughout varying parameters. Moreover, 1 square mechanical rod was printed for each laser power energy and sectioned into five smaller cubes; each one of these cubes received a different heat treatment (Fig. 24). This had the purpose of studying the phases, microstructures, and properties of the material as heat treatment progressed.

Ongoing research has demonstrated the excellent mechanical properties obtained by DED, such as yield strength, ultimate tensile strength, and hardness. [7] DED processes have three branches in which process parameters are generally classified: i) systems specifications dependent, ii) feedstock dependent, and iii) process. [5] In research performed by Simchi [6], results reveal that the sintered density of a material depends on both feedstock properties and fabrication parameters. Processing variables often show that higher laser power corresponds to slower cooling rates that can result in larger grain sizes. Also, as the material feeding rate increases, deposition thickness increases, yielding a coarser microstructure, and finally, the rise in scanning speed improves the thermal gradient fastening cooling rates. [73] Hence, higher density is attained as the laser power increases, and the scan rate decreases. [6] Furthermore, a build's microstructure and mechanical properties also depend on the solid-state transformation that occurs when cooling down to room temperature. These transformations result in consecutive thermal cycles when the laser beam moves along the surface layer by layer and typically. These factors combined normally yield a columnar dendritic morphology. [7] Given the complicated thermal cycling LP-DED samples undergo, the final microstructures generally yielded by this process are irregular and retain high residual stresses; hence, they must undergo a series of post-processing heat treatments. [47]

Table 4. Varying coupon types and build parameters

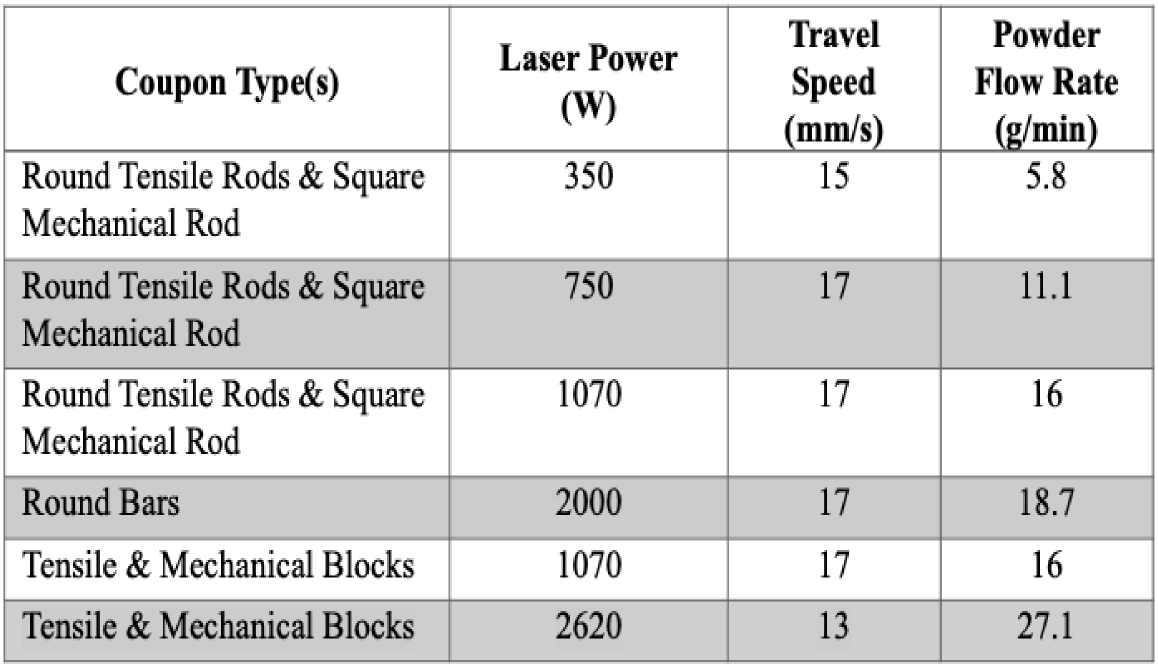

Coupon Type(s)	Laser Power (W)	Travel Speed (mm/s)	Powder Flow Rate (g/min)
Round Tensile Rods & Square Mechanical Rod	350	15	5.8
Round Tensile Rods & Square Mechanical Rod	750	17	11.1
Round Tensile Rods & Square Mechanical Rod	1070	17	16
Round Bars	2000	17	18.7
Tensile & Mechanical Blocks	1070	17	16
Tensile & Mechanical Blocks	2620	13	27.1

Figure 21. Schematic of LP-DED print

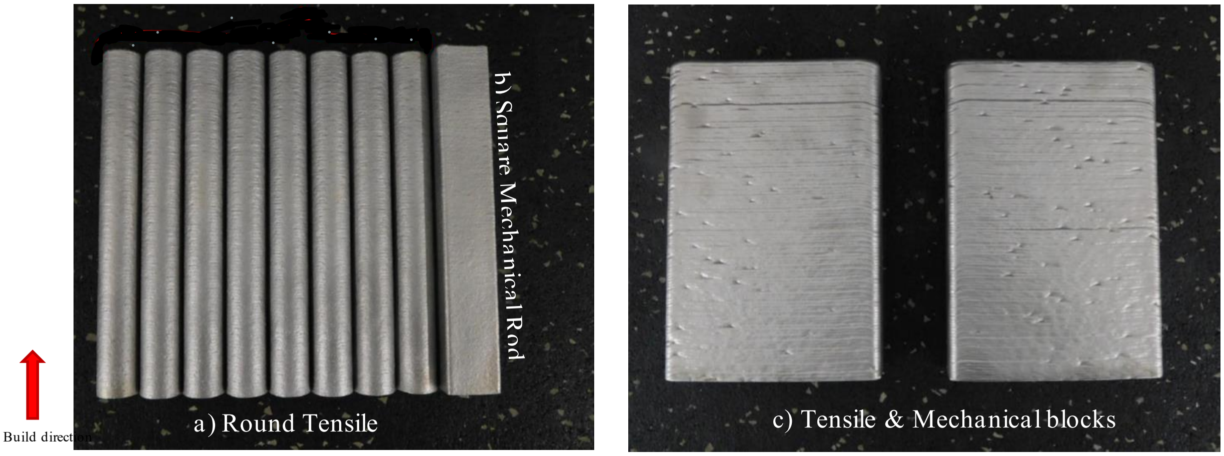

Figure 22. Coupon Types a) round tensile rods b) square mechanical rod c) tensile and mechanical blocks

3.2Post-Processing Heat Treatment

All round tensile rods and tensile and mechanical blocks were post-processing heat treated as per NASA’s standard Inc 718 cycle. This standard involves i) stress relieving (SR) at 1065°C for 1.5 hrs. slow furnace cool with venting to air as soon as allowable, ii) Hot isostatic press (HZ) at 1165°C and 15,000psi for 3 hrs. as per ASTM F3055 / 3301-18a, iii) Solution treatment (ST) at 1065°C for 1 hour, vacuum and argon quench as per AMS 5664 and, iv) Precipitation treatment (aging) at 760°C for 10 hrs ± 0.5 hrs furnace cool to 649°C, hold until a total aging heat treatment time of 20 hours has been reached and cool as per AMS 5664.

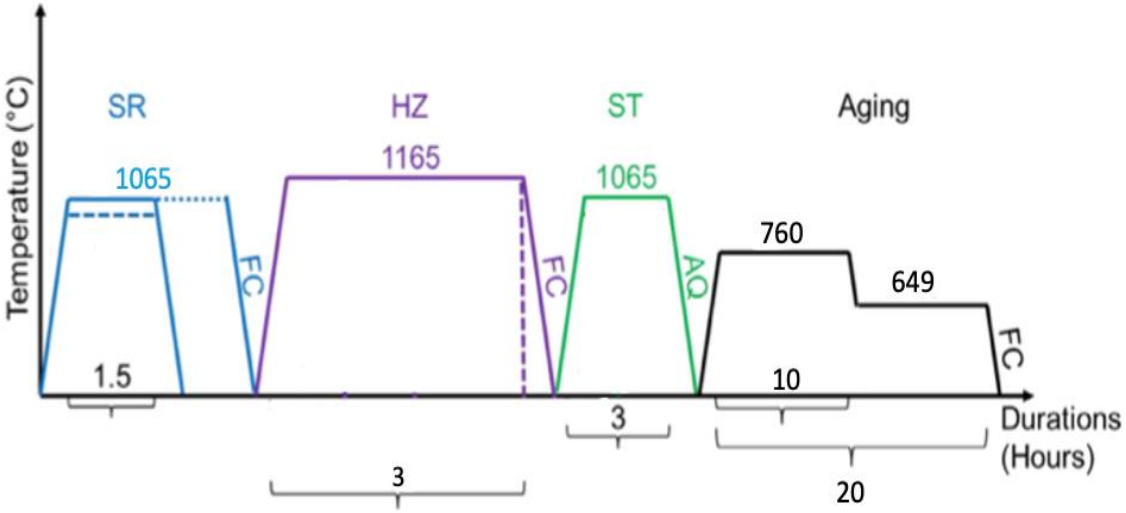

Figure 23. Heat treatment schedule as per NASA's Inconel 718 cycle.

3.3Metallographic Preparation

Each pre-sectioned square mechanical rod was sectioned in the z direction to reveal the build direction microstructure at each stage of the heat treatment with an ATM Brilliant 220 precision cutter. Metallographic samples of the sectioned specimens were created using a combination of powdered epoxy and phenolic acid and a hot mounting press from ATM OPAL. Grinding and polishing were done after the samples were mounted to produce a mirror-like surface. The grinding and polishing procedures were carried out with an ATM SAPHIR 530 semi-automatic system. The grinding procedure was started with a 320-grit coarse Silicon carbide (Si-C) grinding paper followed by grits 400, 600, and 800: each was spun at 150 RPM with a force of 25N for 45 seconds to1 minute using water as a lubricant. The polishing procedure was performed at a speed of 200 RPM and a force of 20 N for

4 minutes, with each stage of the polishing process having a different nylon disk for the 6 µm, 3 µm, and 1 µm diamond suspension slurries. Finally, the samples were polished for 10 minutes at 100 RPM with a force of 18 N using a soft synthetic cloth disk and a 0.1µm colloidal silica slurry.

The etchant used to reveal the microstructures after grinding and polishing was Kalling's #2. The solution was applied to the surfaces with a dropper for varying times from 5 to 120 seconds. The optical micrographs in this work were taken with an Olympus GX53 inverted optical microscope and a Keyence VHX-7000 series.

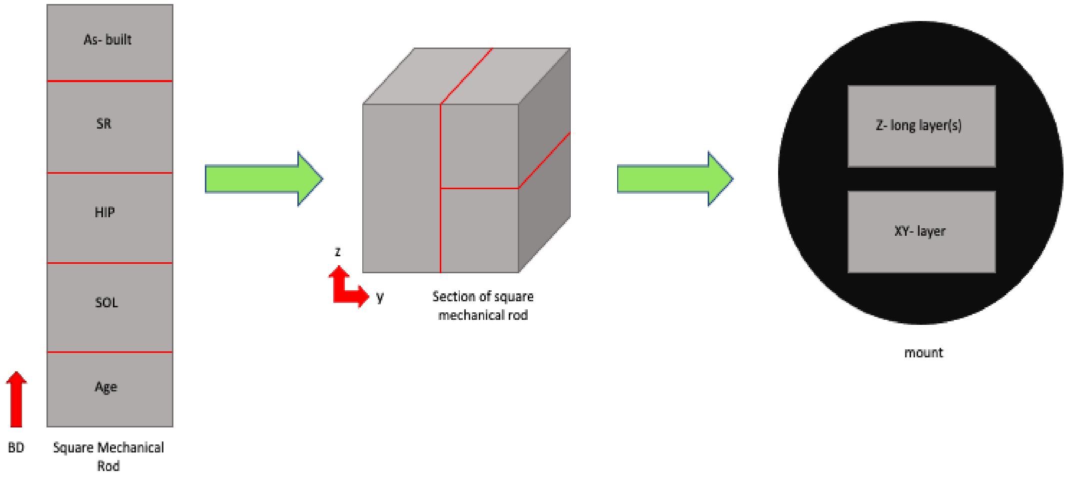

Figure 24. Schematic of mechanical square rod before and after sectioning and mounting.

3.4 Grain Width/Size Measurements

The line intercept method. As per ASTM E112, was used to compute grain width measurements. The software ImageJ was used to draw and measure straight lines across the micrograph this was performed in order to calculate the average grain size of each laser power and compare them.

3.5 Hardness Testing

Micro-indentation Vickers hardness was performed in the as built and NHT condition of the varying laser power samples with a QTAM QNESS 60 M EVO. At least five measurements were taken for each sample variation with a load of 1HV.

3.6 Tensile Testing

Tensile testing was conducted on five round threaded tensile rods (one per laser power) with a length of 102mm and a diameter of 15mm which was performed at Product Evaluation Systems, Inc. in accordance to ASTM E8-21. Tensile testing also included the examination of selected fracture surfaces using scanning electron microscopy (JEOL JMS-IT500 SEM).

Table 5. Test matrix for Tensile testing

Inconel 718 Varaible Parameters

Test	Piece ID	Coupon Type	Parameter Set	Number of Samples	Test Cond Temp (F)
Tensile	2200025-003 to 011	Vertical Round Bars	350 W	4	70
Tensile	2200025-012 to 020	Vertical Round Bars	750 W	4	70
Tensile	2200025-021 to 029	Vertical Round Bars	1070 W	4	70
Tensile	2200025-030 to 031	Vertical Blocks	2000 W	4	70
Tensile	2200025-001 to 002	Vertical Blocks	2620 W	4	70
Total = 20					

3.7Low Cycle Fatigue Testing

To investigate the fatigue properties of Inconel 718 stain controlled low cycle fatigue experiments were performed; Three round tensile rods were selected per laser power for low cycle fatigue testing were these were subjected to tension-compression cyclic loading at a constant strain amplitude of 1% until failure. LCF was conducted at Product Evaluation Systems, Inc. Testing at a frequency of 0.5Hz as shown in Table 3. LCF tests also included the examination of selected fracture surfaces using scanning electron microscopy (JEOL JMS-IT500 SEM).

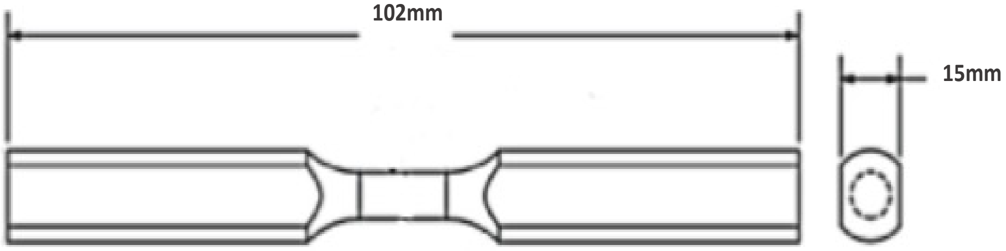

Figure 25. Low cycle fatigue specimen

Figure 26. Test matrix for LCF

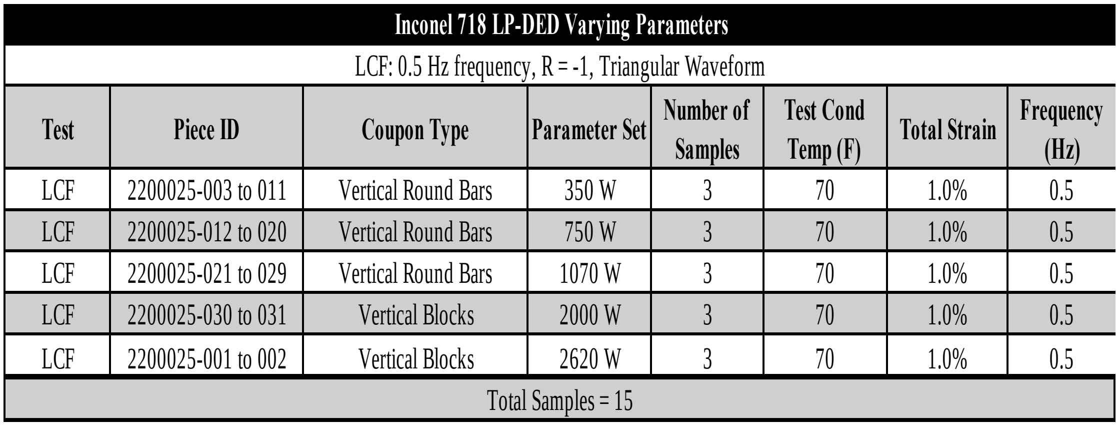
Inconel 718 LP-DED Varying Parameters

LCF: 0.5 Hz frequency, R = -1, Triangular Waveform

Test	Piece ID	Coupon Type	Parameter Set	Number of Samples	Test Cond Temp (F)	Total Strain	Frequency (Hz)
LCF	2200025-003 to 011	Vertical Round Bars	350 W	3	70	1.0%	0.5
LCF	2200025-012 to 020	Vertical Round Bars	750 W	3	70	1.0%	0.5
LCF	2200025-021 to 029	Vertical Round Bars	1070 W	3	70	1.0%	0.5
LCF	2200025-030 to 031	Vertical Blocks	2000 W	3	70	1.0%	0.5
LCF	2200025-001 to 002	Vertical Blocks	2620 W	3	70	1.0%	0.5

Total Samples = 15

CHAPTER 4: RESULTS AND DISCUSSION

4.1 Laser Penetration Depth

The melt pool depth and width were measured for different parameter sets in the NHT condition. As shown in Fig. 27 and 28 the melt pool size increased with increasing laser power as expected.

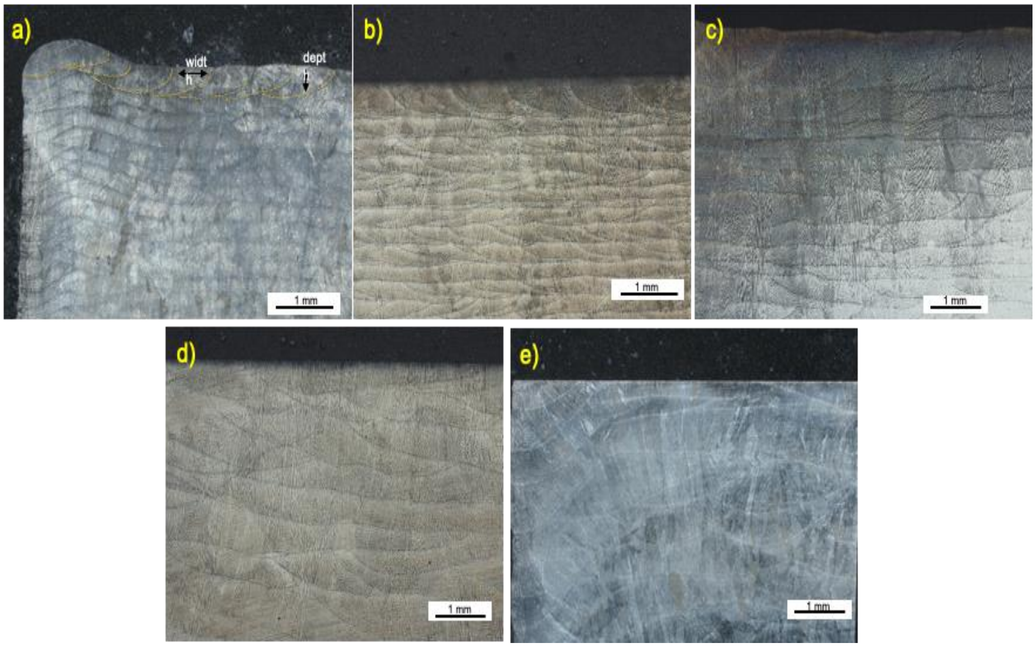

Figure 27. Meltpool morphology for samples built with varying parameters

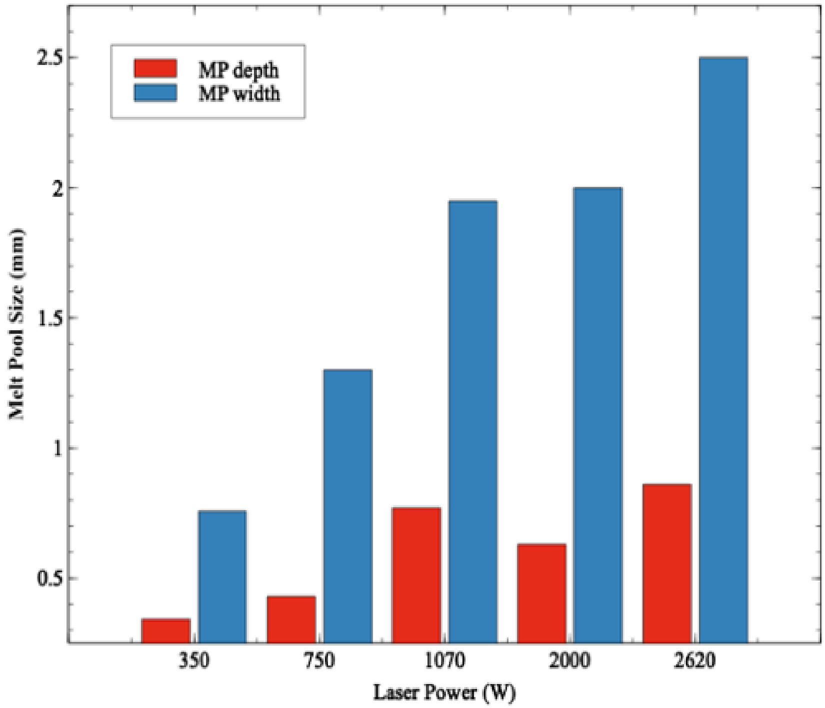

Figure 28. Melt pool depth and width for samples printed with varying parameters

Additionally, the secondary dendrite arm spacing (SDAS) was calculated from the NHT etched samples for each set of parameters using the software image j. These values were obtained by dividing the length of the primary dendrites by the number of the secondary dendrites and taking the average. The cooling rate during Inconel 718 deposition was estimated using the SDAS- cooling rate equation of A286, a Fe-Cr-Ni alloy of similar chemistry to alloy 718 as proposed in Ref. [94]:

$$SDAS = K\left(\frac{dT}{dt}\right)^{n}$$

Where:

K= 31.7 [94]

n= -0.38 [94]

K and n are material dependent constants. Frisk et al. [47] indicated 31.7 and −0.38 for K and n, respectively. The calculated SDAS and cooling rate are shown in Fig. 29(b). Increasing laser power resulted in slower cooling rates.

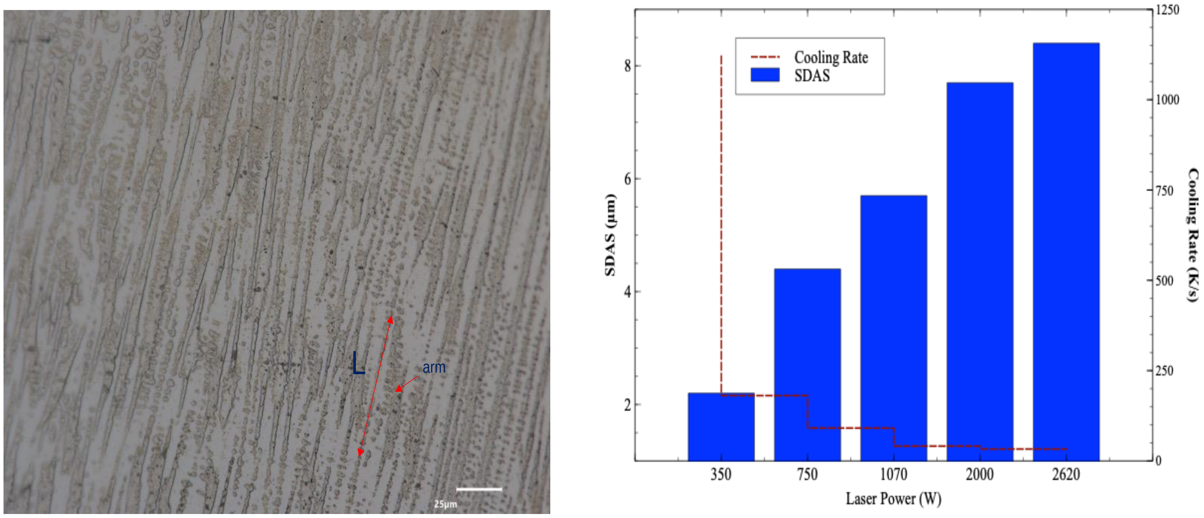

Figure 29. a) ex. of NHT etched sample printed with parameter set 1070 at 1000x with visible dendrites used to calculate SDAS b)) measured SDAS, and calculated cooling rate

4.2 Defect/Density Analysis

The density of 5 samples was evaluated in the NHT condition along the build direction: These resulted in a density higher than 99.5%. The cross sections of the specimens were investigated for porosity, with all specimens reporting values less than or equal to 0.5%. It can be noted that the highest density among all laser powers before heat treatment was that of laser power 1070W at 99.95%. Defects mostly consisted of a combination of gas entrapment and keyholing. Keyholing defects were predominant in the sample printed with 2000W. Additionally, higher porosity volume areas were present towards the walls or edges of the square mechanical rods versus the center of the material as shown in Fig. 32. This has been observed in previous studies [85] and is attributed to irregular heat transfer during the raster process.

However, overall density increased after the completion of the solution-age treatment for samples of all laser powers up to 99.96% with an average of only 0.016% defect area fraction. Fig. 30 and 31 show samples build with 1070W and 2000W in the NHT condition and after being subjected to post processing aging heat treatment to exemplify the reduction in defect area volume. Babamiri et al. [86] found that porosity of Inc 718 decreased after being submitted to HIPing and that as heat treatment progressed the area fraction of voids decreased.

Previous research [87,88] has determined that porosity is dependent on build process parameters such as laser power, powder feed rate, and scan speed. Zhong et al. [39] resolved that porosity decreases with increasing laser power. However, Wolff et al. [41] found that porosity is found at the low and high extremes of laser power energies.

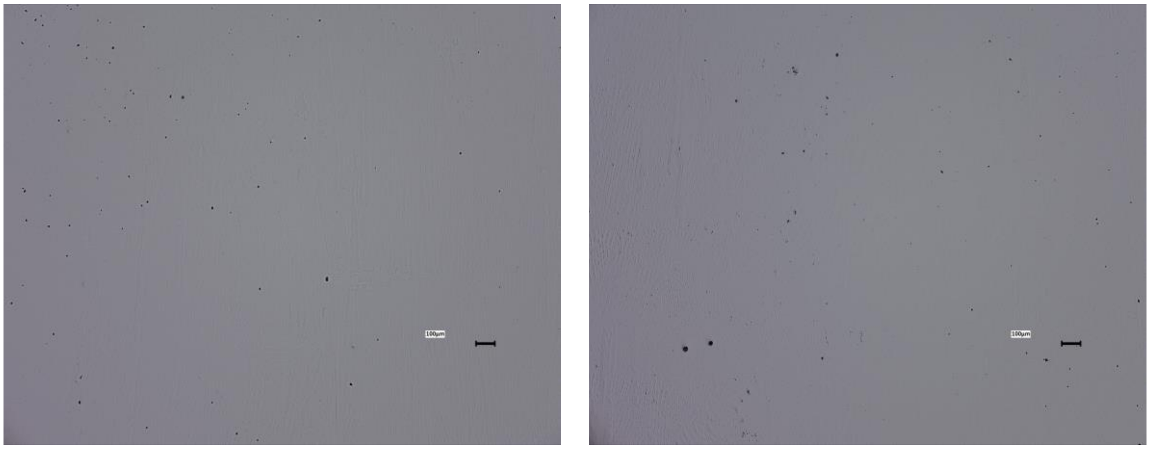

Figure 30. Porosity in samples 1070W and 2000W in the NHT condition

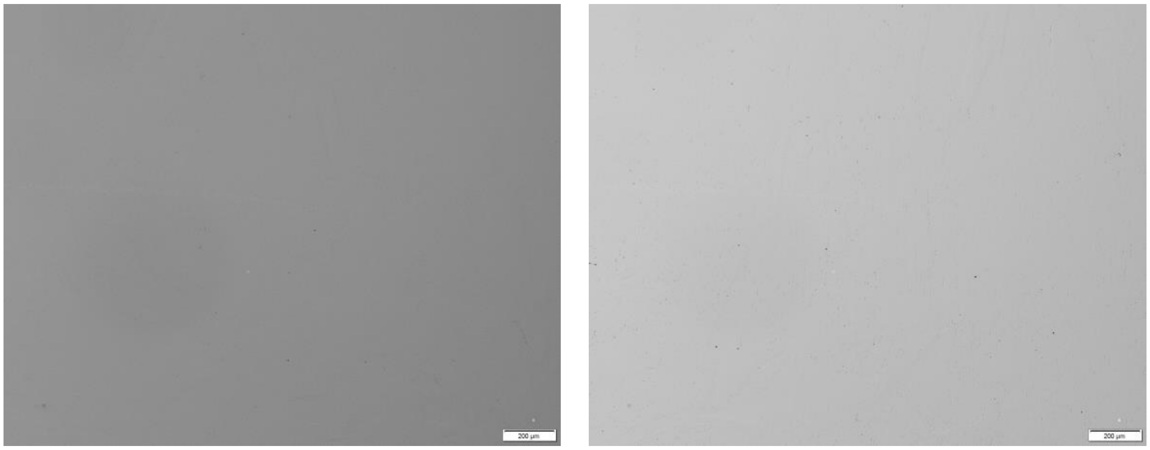

Figure 31. Porosity of samples 1070W and 2000W after HT

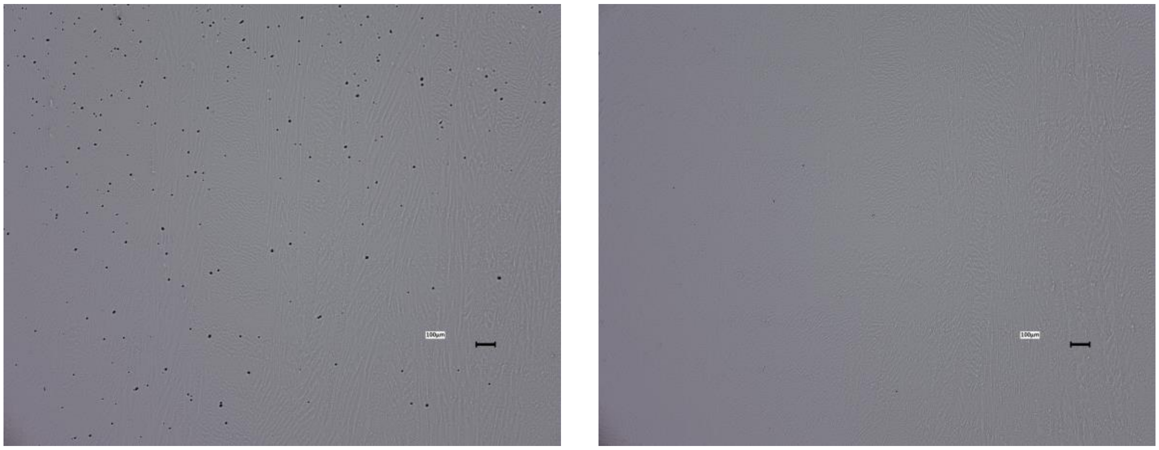

Figure 32. Sample 750W a) near the edge b)bulk material/centre

4.3 As built microstructure

Fig. 35 (a,d,g,j,l) shows the microstructures of laser powers 350W-2620W increasingly in the NHT condition. All samples in the as deposited condition show columnar grains growing epitaxially along the deposition direction with varying arrays of microdendrite structures. Large columnar grains can be observed extending over numerous deposited layers. Melt-pool tracks and layer bands are visible throughout the micrographs; as laser power increases melt-pool tracks seem to grow wider. Moreover, multiple irregular, grayish phases are observed in the inter dendritic regions previously identified as Laves phases. [88] Fig. 36 shows a SEM image of a sample built at 1070W in the NHT condition exhibiting micro segregation or laves phase; although there is no direct chemical evidence, these features resemble micro segregation or laves phase which have been described in multiple studies of Inc 718 fabrication.

Microhardness values varied from 273 HV for the 350 W-fabricated Inconel 718 using LP- DED in Fig. 35a) to 286 HV for 2620 W (Fig.35l). Samples fabricated with laser powers 750W, 1070W, and 2620W had microhardness values of 263HV, 269HV, and 271HV respectively.

It has been determined in previous research that the dendritic morphology for LP-DED Inconel 718 is due to the complicated thermal cycling it undergoes during printing: the deposited material experiences remelting, re-solidification, and solid-state phase transformation depending on factors such as heating rates, cooling rates that can reach up to 10^3-10^5K/s, thermal gradients, number of thermal cycles, etc. [8]. Bontha et al. [54] established the relationship between dendrite morphology, temperature gradient (G) and solidification velocity (R) during the DED process. According to this previous research [31, 54] the typical as-built microstructure of a 718 printed sample consists of columnar dendrites which usually grow in the <1 0 0> orientation parallel to the deposition. The columnar morphology extends through the deposited layers due to re-melting of previous layers and heterogeneous nucleation of γ dendrites.

Table 6. Grain width measurements for samples printed at varying laser powers at varying HT

Grain width (µ)	**HT**	**SR1065/1.5**	**HZ1165/3**	**ST1065/1**	**Aged**
	Laser Power				

	350W	138	148	111	104
	750W	191	164	154	118
	1070W	211	217	198	122
	2000W	163	276	209	124
	2620W	155	239	206	146

Figure 33 shows the XRD spectra of NHT and HT samples along the build direction. The XRD spectra shows enhanced {111} and {200} texture along the build direction for NHT samples. Further, the spectra for HZ and aged specimens indicate a preferential {111} with no other significant peaks this however could be

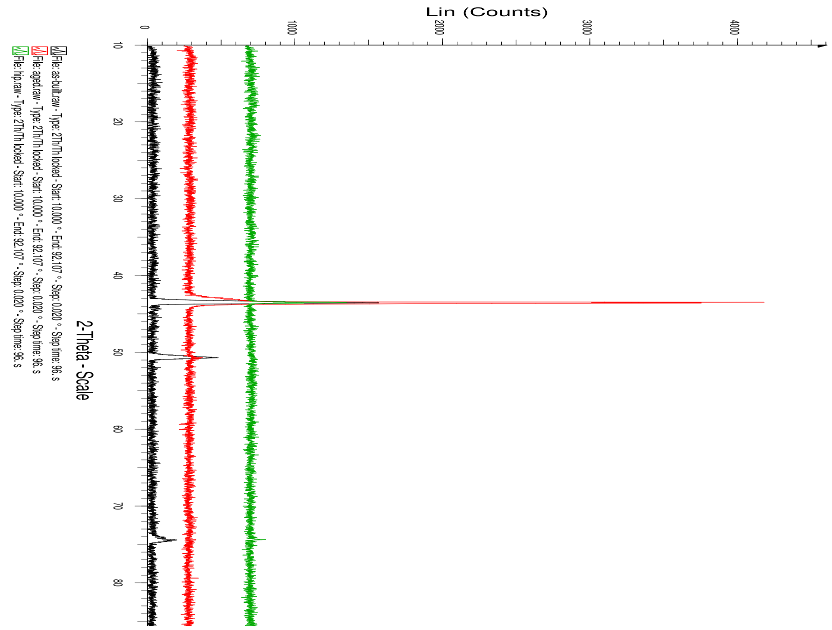

Figure 33. XRD spectra of Inc 718

due to a lower volume fraction of other phases. Therefore, further investigation to identify if other phases existed in the HZ and aged specimens was needed.

4.4 Effect of Heat Treatment on Microstructure

Traditionally, Inconel 718 is subjected to a solution heat treatment to dissolve segregation particles into the matrix, and aging is performed to precipitate the strengthening phases γ′ and γ’’. [43] However, the DED processes are different from traditional manufacturing, hence the effects on post processing heat treatments on the microstructure of alloy 718 need further observation.

Figure 35 shows samples produced with laser powers 350W-2620W after HZ (b,e,h,f,m) and double aging (c,f,I,k,n). The optical micrographs (b,e,h,f,m) indicate that following HZ treatment, melt pool traces diminish in the build direction, nearly disappearing when compared to the as fabricated samples. Grains in the range of 148 µm for 350W to 277 µm for 2000W with hardness values of 249 HV and 225 HV respectively are observed with visible precipitates. This trend exemplifies that grain size increases with the increase of laser power. Moreover, partial recrystallization of the dendritic structure into a combined microstructure of coarser irregular and columnar grains is shown after HZ performed at 1165°C for 3 hours. Heat treatments above 1100°C have shown to induce recrystallization of AM IN718 [89]. For example Chlebus et al. [89] performed a 1 h 1100°C heat treatment on L-PBF IN718 which resulted in a recrystallization and homogenization of the γ solid solution with carbides observed at grain boundaries.

Micrographs of the microstructures after aging (c,f,I,k,n) show a fully recrystallized equiaxed microstructure containing annealing twin grain boundaries with densities of {111}. Twin boundaries started developing during HZ but increased after ST and aging meaning complete recrystallization and growth of all microstructures after double-aging treatment. Fig. 34 contains the grain average measurements for each laser power specimen calculated by the intercept method. Samples fabricated with laser power 350W had a smaller grain size overall with an average of 104 µm and a respective hardness of 463 HV and the sample printed with a laser power of 2000W had the largest grain size in the aged condition measuring 157 µm with a respective value 458 HV. However, microstructures at all different laser powers exhibit a similar trend whereas exposed to a HT > 1000°C the dendritic morphology developed into a recrystallized-combined microstructure of equiaxed and columnar grains.

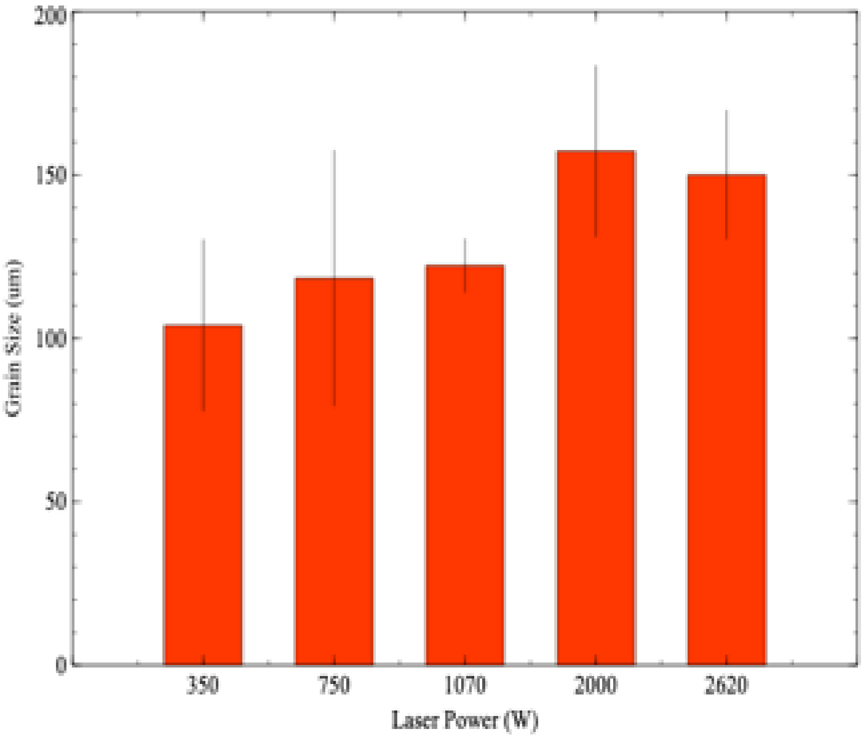

Figure 34. Grain size vs Laser Power in the aged condition

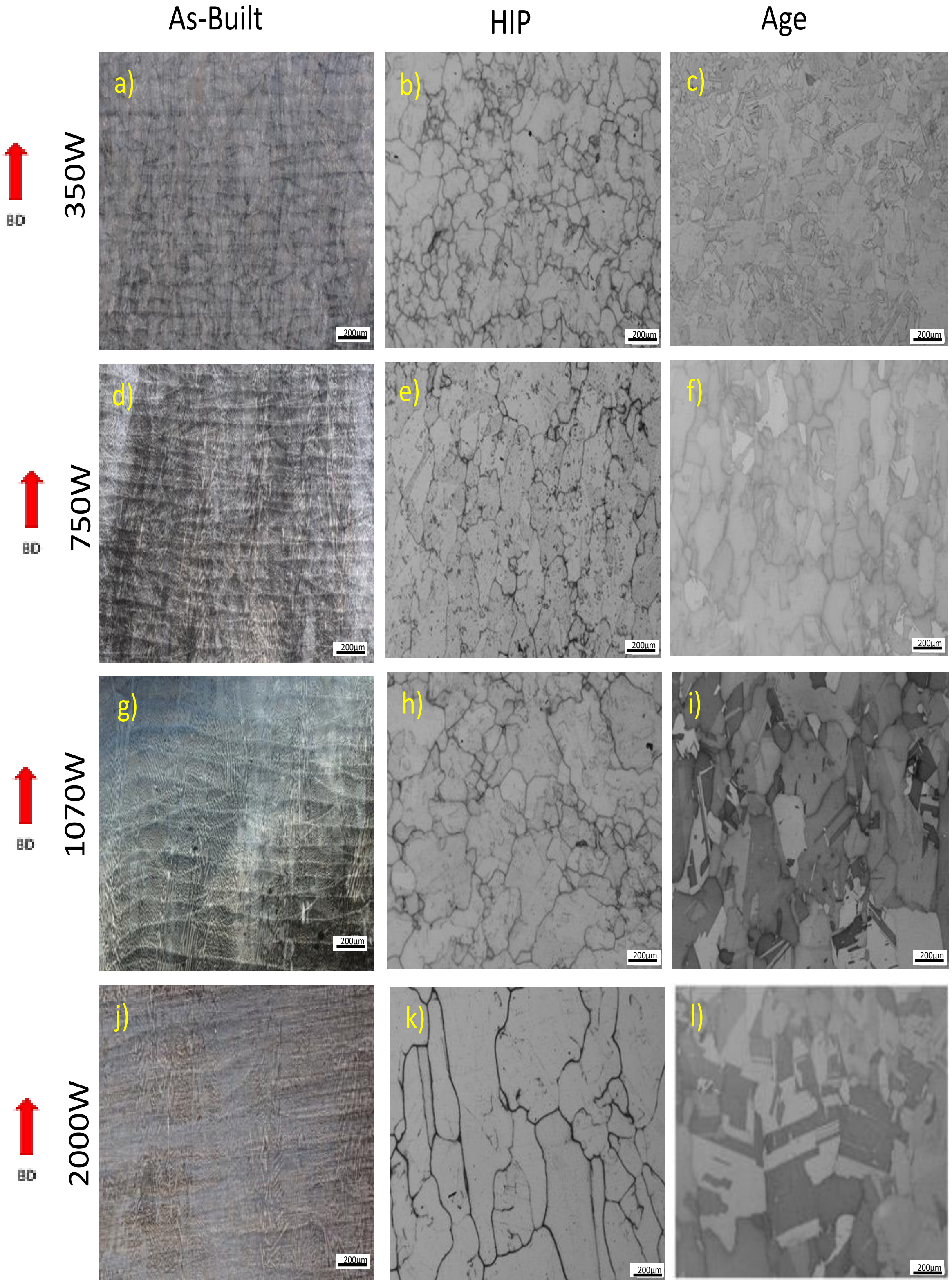
As-Built
HIP
Age
350W
BD
a)
b)
c)
750W
BD
d)
e)
f)
1070W
BD
g)
h)
i)
2000W
BD
j)
k)
l)
200µm

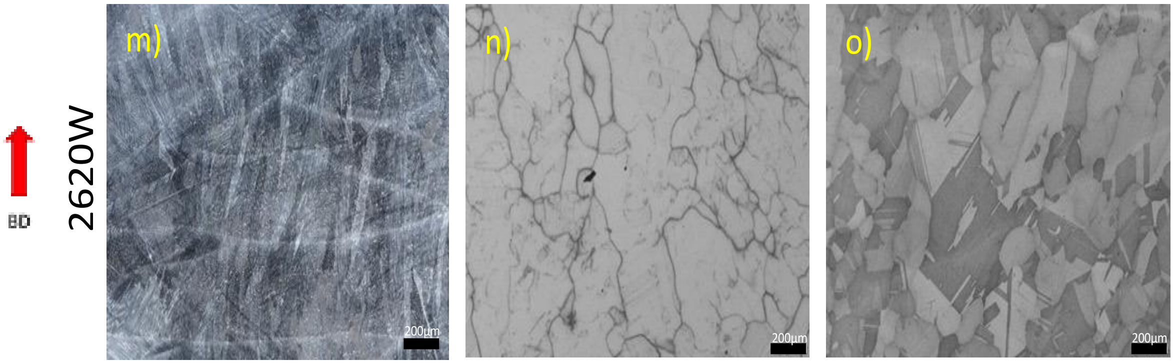

Figure 35. Microstructures of samples printed with varying laser powers in the NHT,HZ, and aged conditions from left to right.

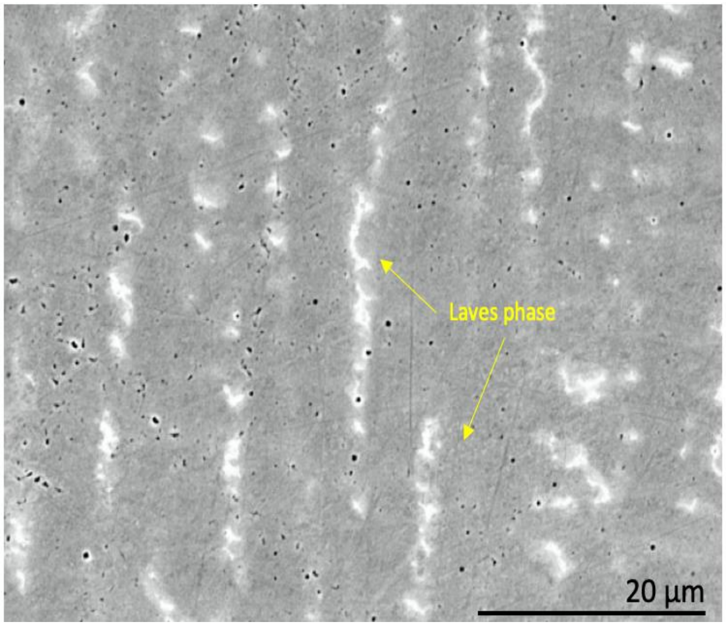

Figure 36. Laves phase in the NHT condition in sample built with 1070W

4.5 Mechanical Properties

4.5.1. Hardness (HV)

Hardness values were measured from all samples built with varying parameters and at each stage of the HT schedule in the build direction. The NHT samples hardness values centered around ~275 HV, these values are similar to as deposited hardness values found in research [90] by Galarraga et al. There was a hardness increase from the NHT condition to the SR condition obtained and corresponded with the precipitation of strengthening phases γ′ and γ″.[90] An expected drop in hardness shown in Fig. 7 from the SR to the HZ and SOL conditions could be attributed to the dissolution of some precipitates during homogenization [2,90] and to the sharp increase in grain size that can be observed in the HZ condition in Fig 35.

Moreover, after HZ a ST was performed where the samples were heated above the solution temperature (1065°C) to ensure the dissolution of all precipitates and argon quenched to room temperature to avoid grain growth and precipitate nucleation. This justifies the lower hardness values for the HZ and ST conditions as compared to others. Finally double aging was performed to form precipitates in the matrix that would strengthen such. Precipitation treatment was performed for a total of 20 hours. First, 10 hours at 760°C, furnace cooled to 649°C and held at this temperature for 10 more hours, then air-cooled to RT. The increase in hardness after aging can be justified by the formation of primary, secondary, and tertiary γ’ precipitates. Hardness increased 69% from the NHT condition to the final double aged condition.

It can be noted that not all samples were compliant with the hall-petch equation as samples with larger grains than other’s achieved higher strengths. While grain boundaries can contribute to the overall strength, precipitation of secondary phases and solid solution strengthening are the most important strengthening mechanism for Inconel 718. [91]

Table 7. HV values for varying laser powers in the NHT, SR, HZ, ST, and aged conditions

Hardness (HV)	**HT** **Laser Power**	**NHT**	**SR1065/1.5**	**HZ1165/3**	**ST1065/1**	**Aged**
	350W	273	366	249	185	463
	750W	263	342	225	187	464
	1070W	269	385	209	174	451
	2000W	271	388	225	174	458
	2620W	286	363	216	175	471

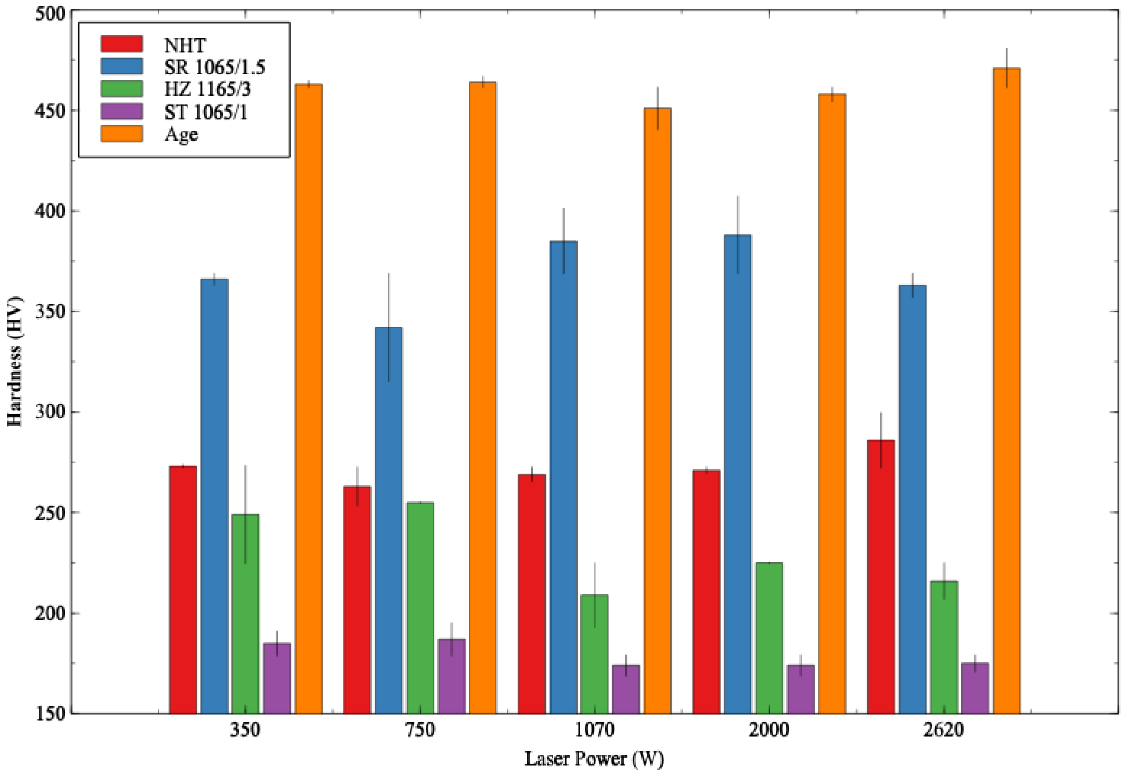

Figure 37. Schematic of HV values for varying laser powers in the NHT, SR, HZ, ST, and aged conditions

4.5.2. Tensile Properties

Tensile properties for samples printed with laser powers 350W-2620W are included in Fig. 38 and Table 10. Complementary, Fig. 40 contains fracture surfaces for all previously mentioned tensile samples. All samples were subjected to the same ST-age post processing heat treatment. A statistical model was run with these properties to determine if the difference between these were negligible. According to statistical data, samples printed with 1070W and 2000W have similar yield strengths. Further it was also proved statistically that samples at 750W and

2620W and 1070W and 2000W have similar ultimate tensile strengths. Tensile samples printed with laser power 350 demonstrated the highest YS and UTS. As laser power increased to 2000W tensile properties decreased but at 2620W increased slightly. The higher tensile properties of samples printed with 350W can be attributed the smaller microstructure produced by higher cooling rates during deposition. Additionally, tensile properties of wrought Inc 718 which is commonly cold- or hot worked are proportioned for comparison. As seen in Table 10 all LP-DED processed samples exhibit higher tensile properties than the wrought material.

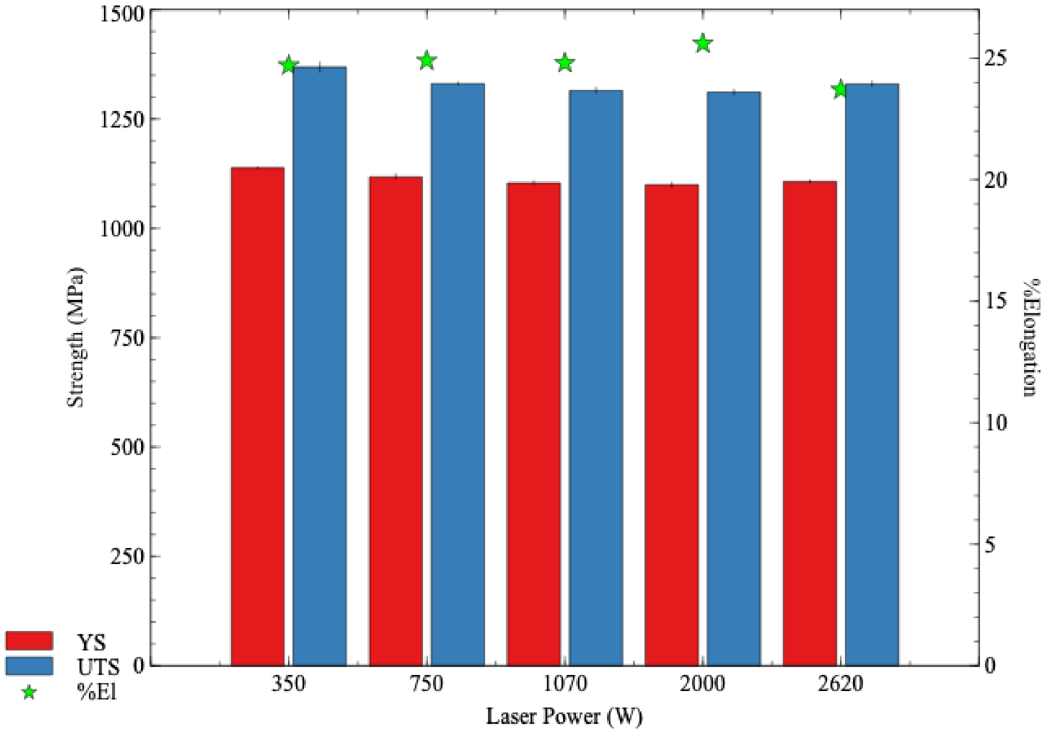

Figure 38. YS, UTS, and %Elongation for samples printed at varying laser powers

Table 8. Tensile values for samples printed at varying laser powers

Laser Power (W) **Tensile Property**	**350**	**750**	**1070**	**2000**	**2620**	**Wrought** [75,76]
YS (Mpa)	1138.3	1117.6	1103.8	1099.7	1106.6	1035-1160
UTS (Mpa)	1368.6	1330.6	1314.8	1311	1330	1100-1400
%El	24.7	24.9	24.8	25.6	23.7	12-21

Further, one tensile bar was selected per laser power to be evaluated in a JEOL JMS-IT500 SEM system. SEM images showed ductile features for all samples such as ductile dimples with sizes ranging between ~1.9 and ~3.9µm. All samples presented ductile fracture mechanism however, the sample deposited with 350W exhibits a larger volume of smaller dimples and microvoids, indicating higher ductility. [65] This is corresponding to its smaller grains and superior tensile properties. The 69ractography showing the fracture surface of the sample printed with 2000W exhibits the largest dimples measuring ~5µ. Figure 39 shows how as laser power increases, dimple size increases up to 2000W where dimple size slightly decreased with 2620W. Supporting the tensile data presented before. These features coincide with the according grain measurements and tensile properties of each ex., 104µ and 1138 Mpa (YS) at 350W versus 157µ and 1099Mpa at 2000W.

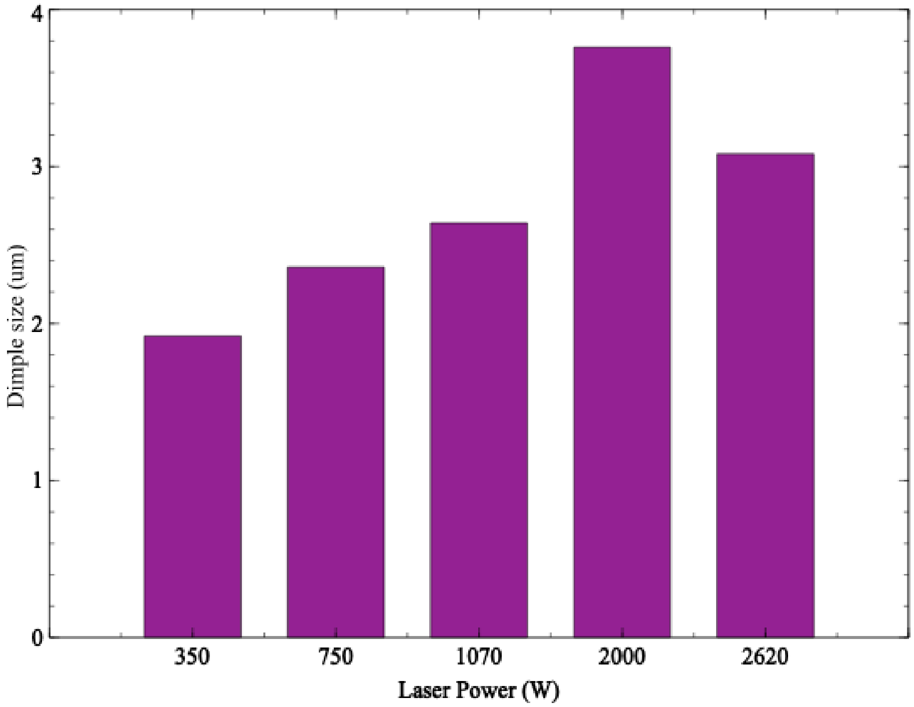

Figure 39. Varying dimple sizes from tensile micrographs

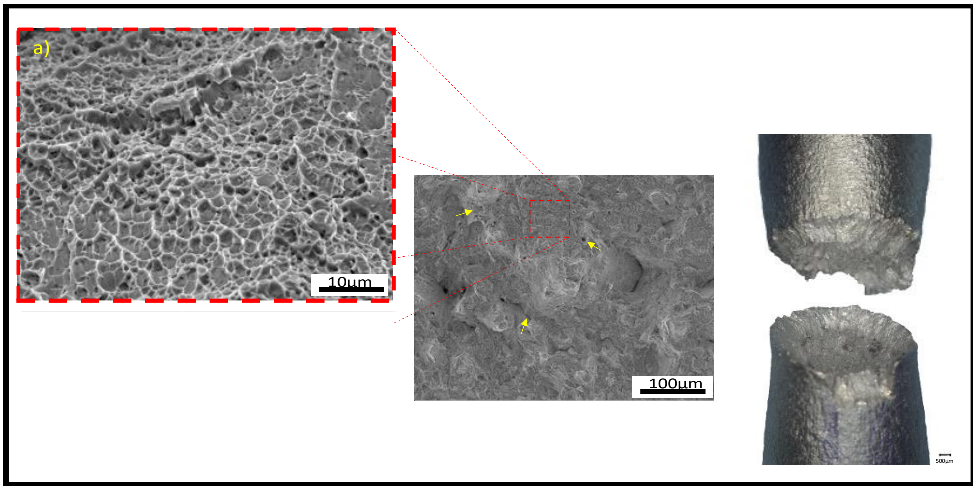
a)
10µm
100µm
500µm

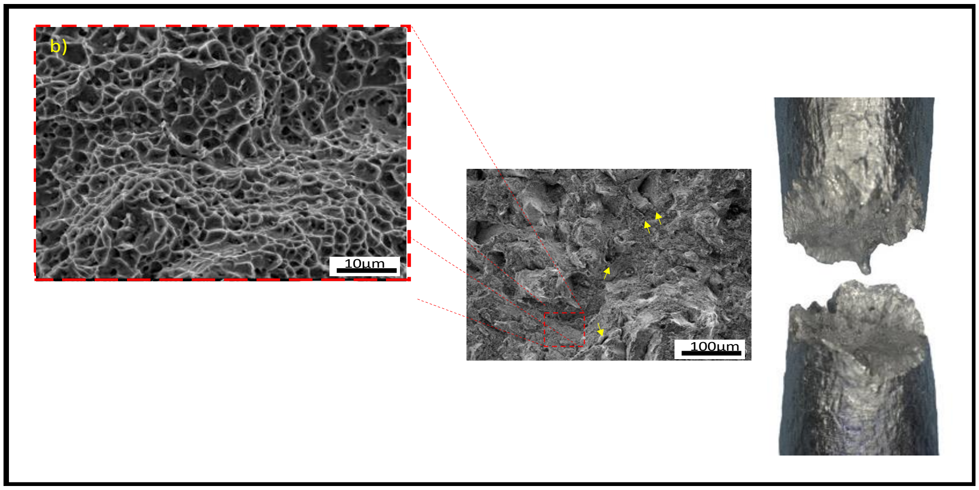
b)
10µm
100µm

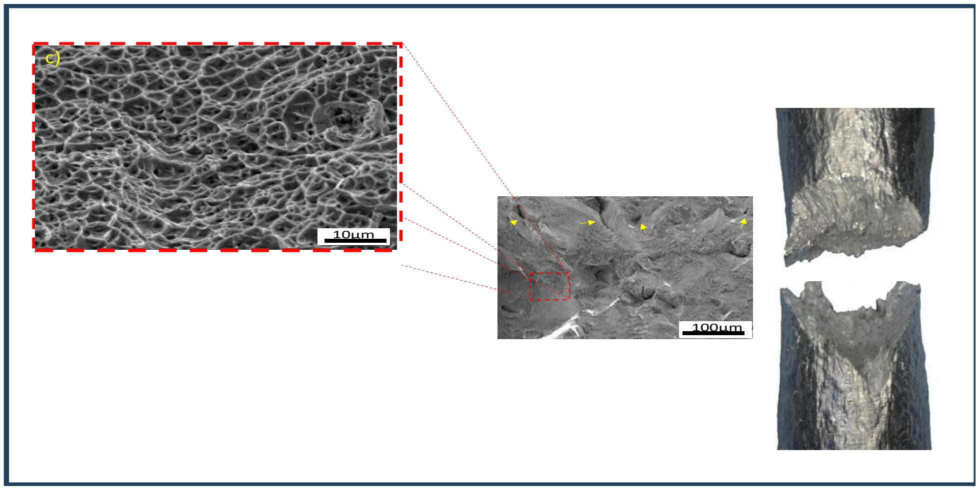
c)
10µm
100µm

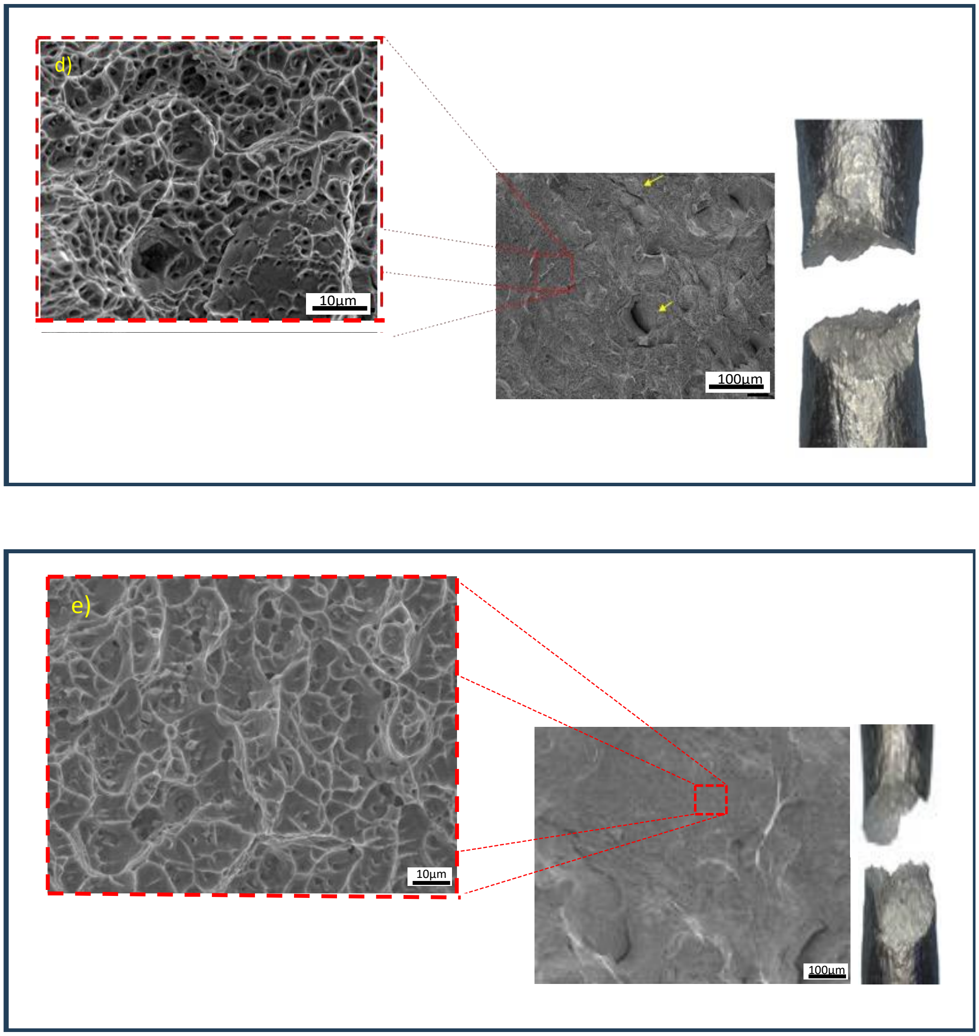

Figure 40. SEM fractographic images for fracture surfaces of tensile samples printed at a)350W, b)750W, c)1070W, d)2000W, and e)2620W. Yellow arrows are pointing to porosity and secondary cracking

4.5.3. Low Cycle Fatigue

All 15 LCF samples were tested in specimens of 3 samples per each laser power. The number of cycles to fatigue for specimens printed with laser powers 350W, 750W, 1070W, 2000W, and 2620W is represented in figure 41 as a box plot. The effects of laser power on fatigue life don't seem to follow a trend, however samples printed at 350W averaged the highest number of cycles to failure followed by specimen printed at 750W this is consistent with both specimen's superior yield strengths.

The fracture surfaces of one selected sample per laser power were examined and are shown in figure 43 and are paired to their respective number of cycles to failure in figure 42.

All fatigue specimens regardless of laser power had failure initiated from the surface or from gas entrapped pores near the surface resulting in final fatigue failures. Fatigue fractographs consist of i) crack initiation(s), ii) crack propagation, and iii) final rupture. In this case, crack intitation is highlighted in yellow, and crack propagation and final failure are separated by a yellow dashed line. Stage two or crack propagation is the largest section in all fractographs and it is characterized by "river marks" these features are the consequence to the repeated stress application and appear as parallel "wavy" lines. These marks indicate the crack growth direction which is perpendicular to loading. The final rupture area is usually opposite to the initiation site; dimples were noted in this area indicating a final ductile rupture mechanism with microvoid and dimple coalescence.

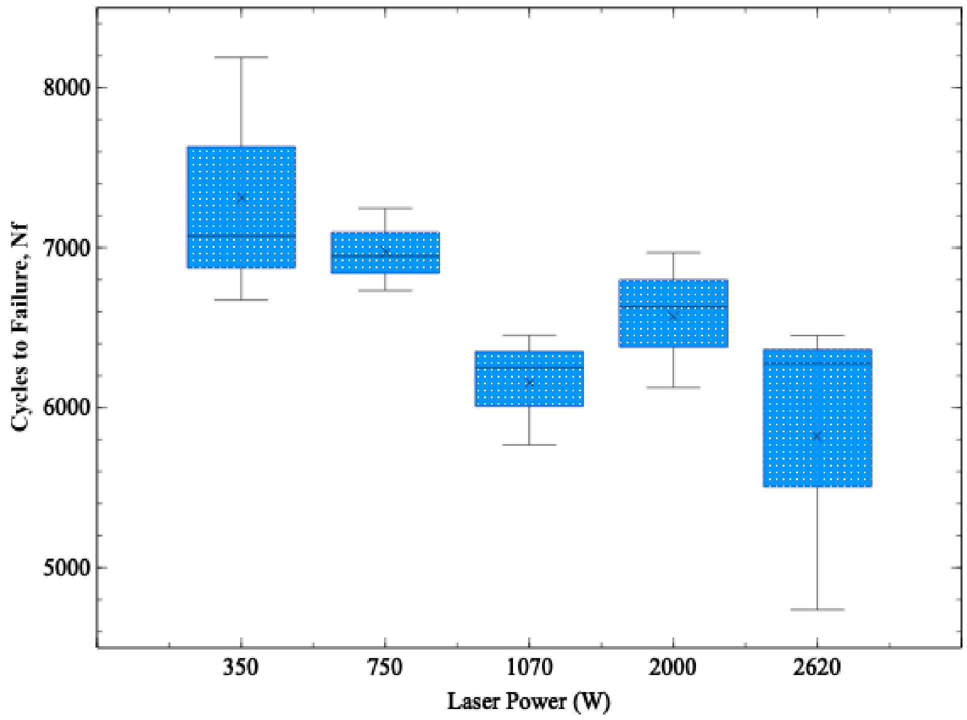

Figure 41. Box plot of average of 3 LCF samples per laser power

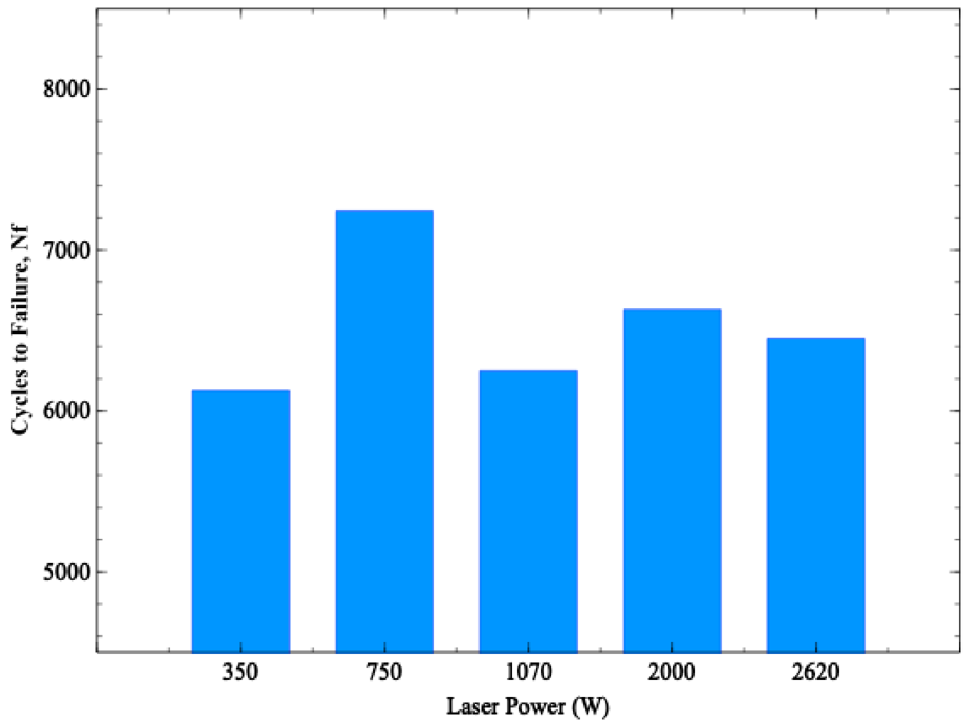

Figure 42. Bar graph of fatigue life of one sample per laser power. Fractography is shown for these in figure37.

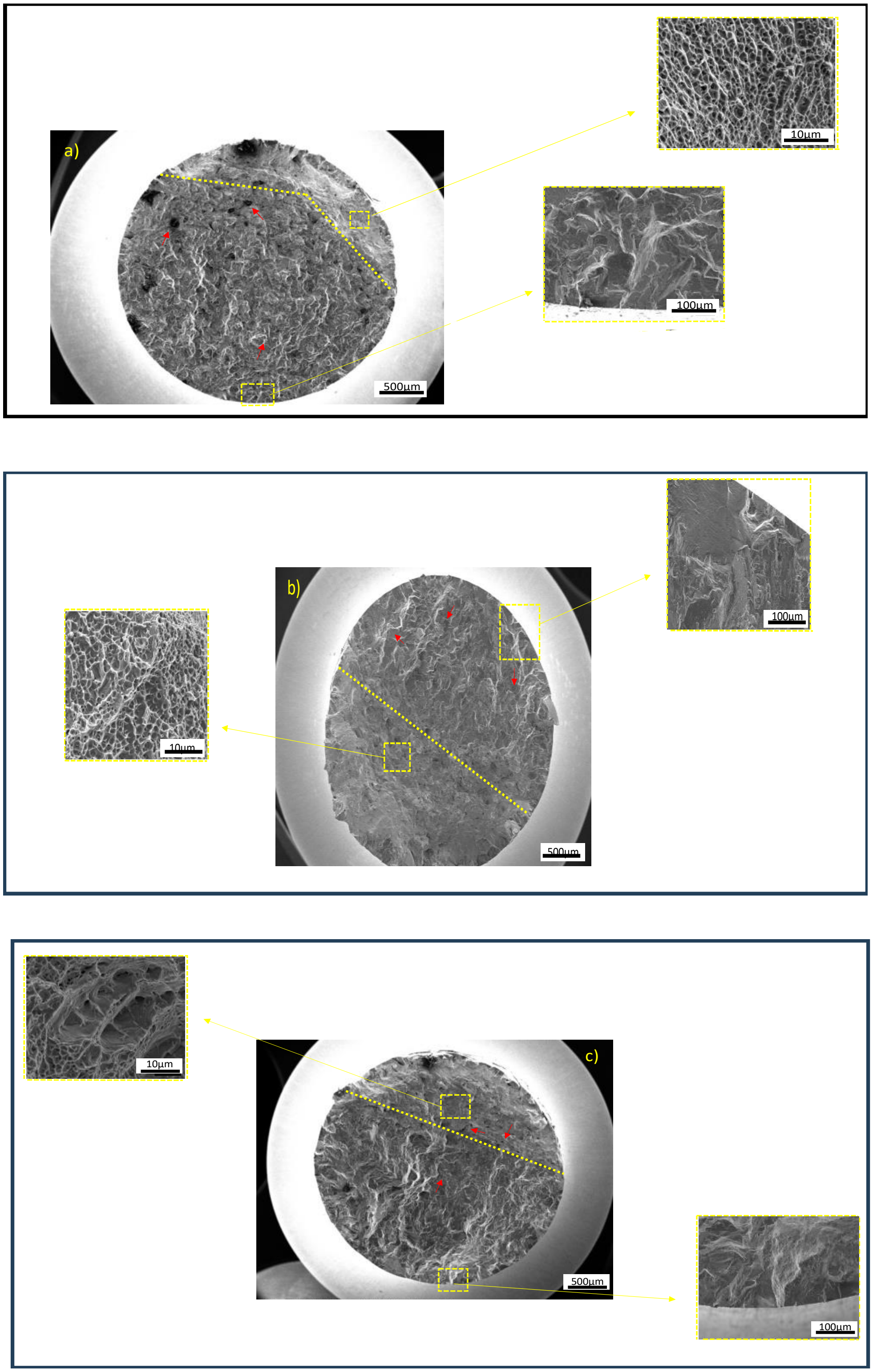

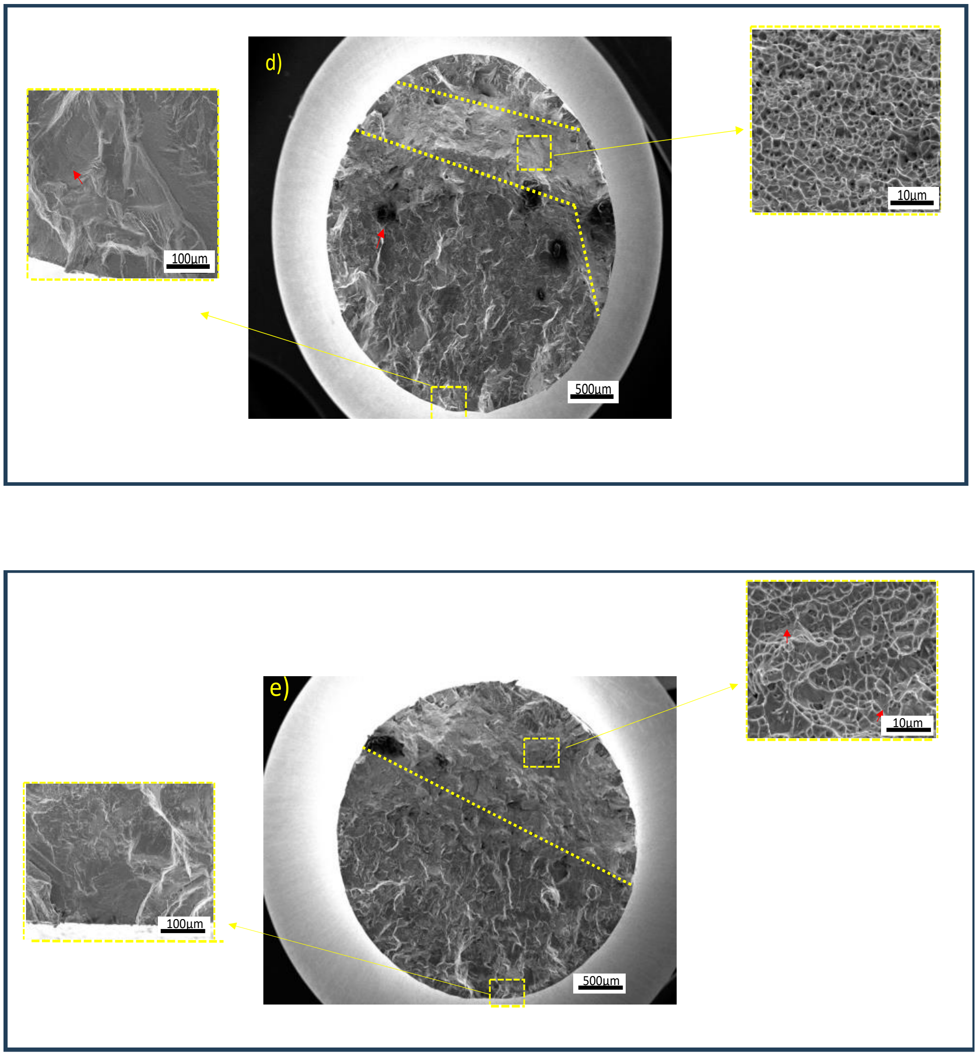

Figure 43. SEM fractographic images for fracture surfaces of LCF samples printed at a)350W, b)750W, c)1070W, d)2000W, and e)2620W. Initiation site(s) are highted in yellow, crack propagation and final rupture sites are separated by yellow dashed line. Red arrows are pointing to porosity, surface defects, crack growth direction and straition.

4.6 Statistical Analysis

Statistical analysis is an essential aspect of a research study as it helps draw valid conclusions from data by identifying trends and relationships and quantifying uncertainty and variability. From different statistical techniques, predictions can also be made for future works. [95] In this investigation, Minitab, a specialized statistical software, is used to assess the relationship between different printing parameters and the resultant mechanical properties of the printed specimens. The ANOVA main effect and 95% confidence plots and other analytical methods are utilized. These plots are valuable tools for visualization and understanding how each variable contributes to the built's observed mechanical properties.

The ANOVA test, a key tool in our analysis, helps determine if there are any significant differences between the means of three or more groups by analyzing its variance. This test produces an F-statistic value and a p-value. If the p-value is below the predetermined significance level (in this case 0.05) this would indicate that there are significant differences between the group means. The F-statistic value represents the variance between group means and between groups. A high F-value suggests there is a significant difference between at least two of the group means.

An additional post-hoc or turkey's significant difference (HSD) test was performed to determine which specific groups are different. Tukey's HSD test identifies which group differences are statistically significant by comparing the differences between group means to a critical value. [97] Various data groups were analyzed, including yield stress, UTS, %Elongation, HV, grain size, and fatigue life of specimens produced with different parameters.

4.6.1 Tensile Properties

Fig. 44 shows the main effect plots for the tensile properties of tensile coupons built with varying parameters yet subjected to identical heat treatment schedules. This comparison assesses whether homogeneous properties can be achieved across these variations.

A significance value of 0.05 was determined for each tensile property ANOVA, where the null hypothesis states that all means are equal. ANOVA results indicated a significance level (p-value) of 0.00 for yield stress and UTS, ruling out the null hypothesis, meaning all means are unequal. Additionally, an F-value of 67.03 was obtained for yield stress, suggesting a significant difference between at least two of the means. The F-value obtained for UTS was 44.28, implying that at least two of the means also have a considerable difference. The p-value for %elongation was 0.032, and the F-value obtained was 3.54. These two suggest less variance within the different group's means. However, the significance level was unmet, and the null hypothesis was rejected. From the main effect plots (Fig. 44), we can determine that both YS and UTS achieve their highest means when produced with laser power 350W and their lowest means when produced with 2000W. The main effects plot for %elongation shows the highest %elongation means for samples built with 2000W, indicating the highest flexibility, and samples built with 2620W show the least.

Additionally, a trend is observable in both UTS and yield strength main effects plots. As laser power increases up to 2000W, both tensile properties decrease and pivot when laser power increases to 2620W.

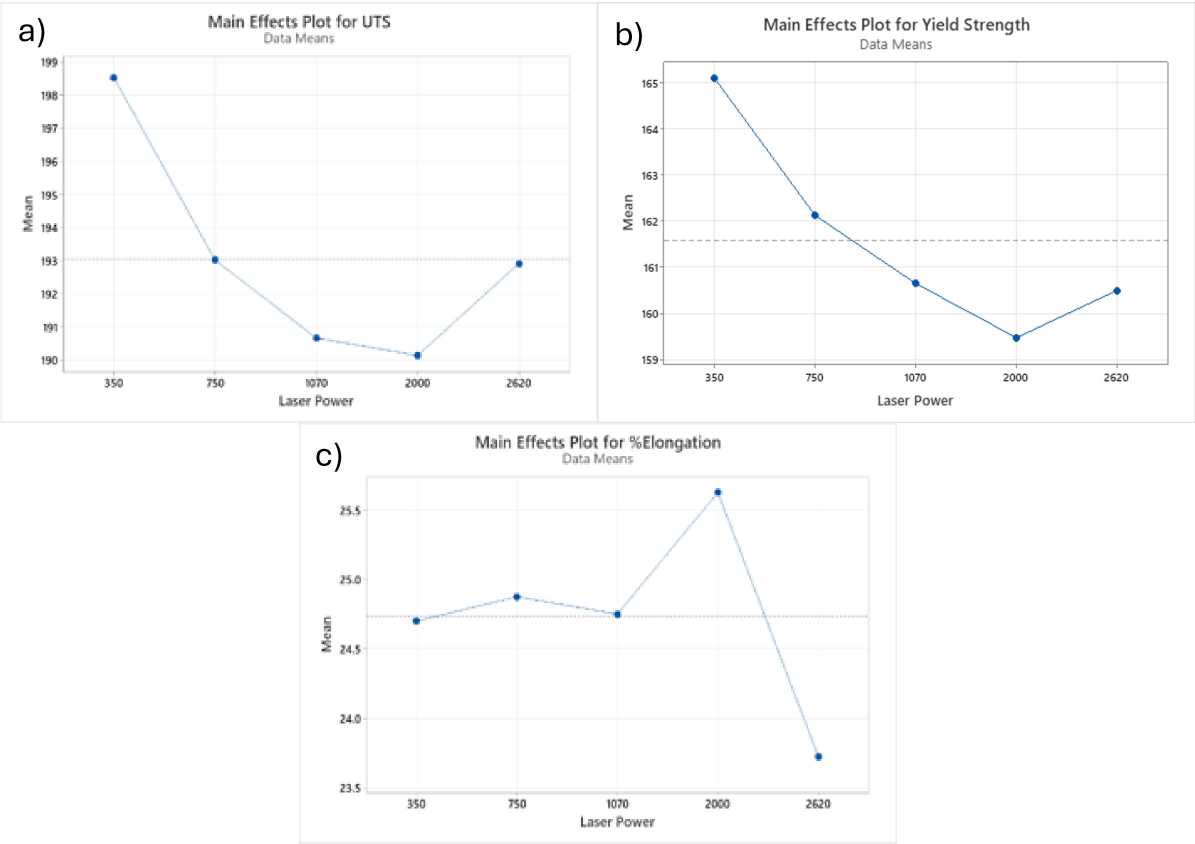

Figure 44. Main effect plots for tensile properties of fully heat treated tensile samples built with different parameters. a) main effects plot UTS b) yield stress c) %Elongation

After the null hypothesis was ruled out for UTS, yield strength, and %elongation, a more in-depth analysis was developed to observe if there would be any groupings or similarities between the different means. Fig. 45 shows Turkey's significance difference test plots where the corresponding means are significantly different if an interval does not contain zero. Based on these plots, we can determine similarities between each tensile property.

For yield stress values, samples printed with laser powers 1070 and 2620 and 2620 and 2000 are not significantly different. Moreover, from Fig. 45a) groupings can also be made where UTS samples printed with laser powers 750 and 2620 and 1070 and 2000 are not significantly different. Lastly, a p-value of 0.032 was obtained for %elongation. This value suggests more groupings or similarities between %elongation means. Fig. 45c) shows that samples printed with laser powers 2000, 750, 1070, and 350 have similar elongation as well as samples 750W, 1070W, 350W, and 260W.

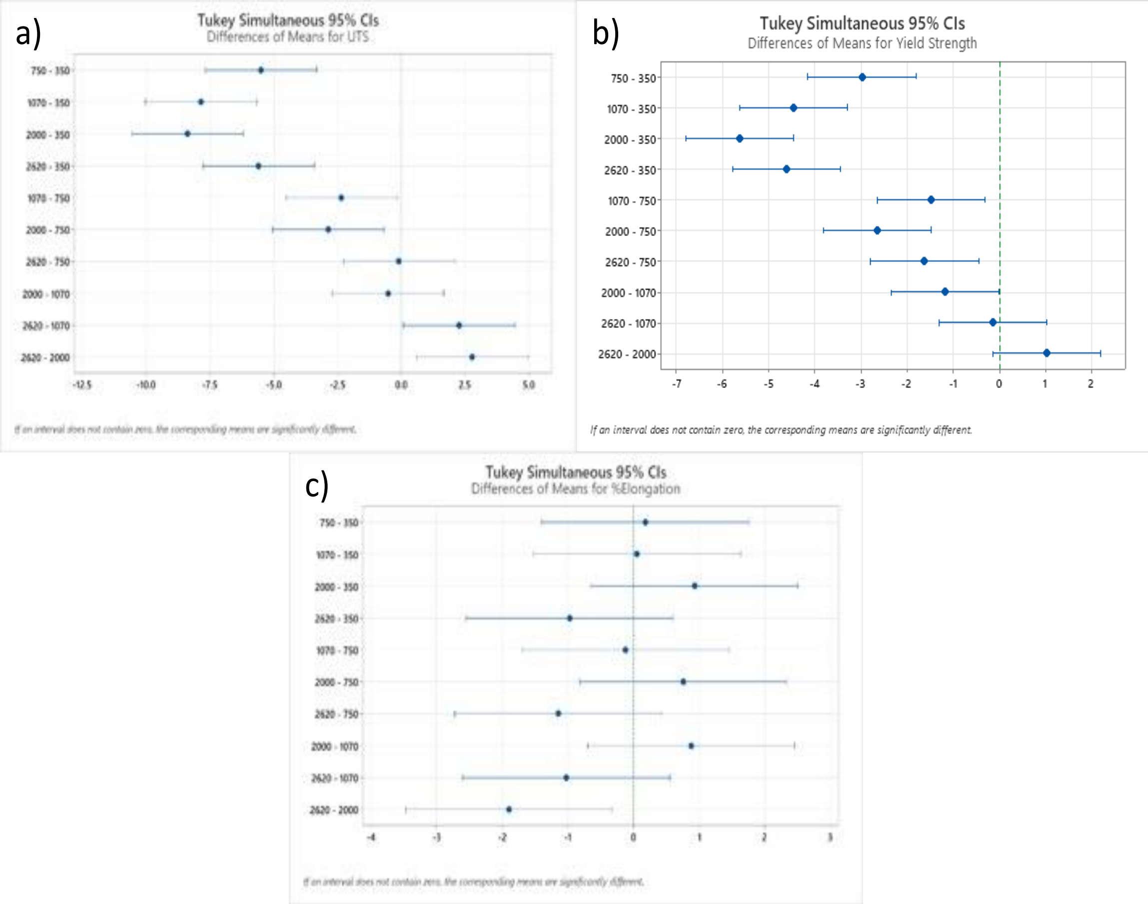

Figure 45. Turkey's significance difference test plots for tensile properties

4.6.2 Fatigue Life

An ANOVA test was performed for the data of fatigue samples built with varying parameters but post-processed with the same heat treatment.

A significance value 0.05 was determined where the null hypothesis states that all means are equal. The p-value obtained for the fatigue life of all specimens equaled 0.077, and the F-value was 2.93. Thus, more evidence is needed to rule out the null hypothesis and conclude that all fatigue life means are equal.

.Fig. 46 shows Turkey's significance difference plot and the 95% confidence test plot. From Fig. 46b), we can observe how specimens printed with laser power of 350 and 750 averaged the highest number of cycles to failure. Cycles to failure appear to decrease discontinuously after laser power increases to 1070W, with samples printed with 2620W achieving the most minor cycles to failure. However, Turkey's significance difference plot (Fig. 46a) proves that all groups are similar. Based on these plots, it can be concluded that the applied heat treatment effectively homogenized the fatigue properties among specimens built with varying parameters

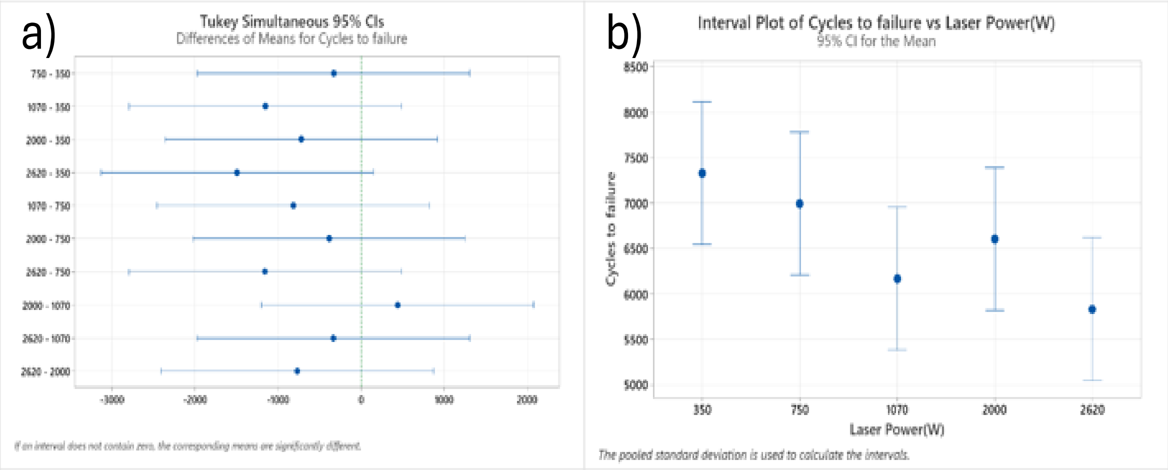

Figure 46. a) Turkey's significance difference plot for fatigue specimens and b) 95% confidence test plot

4.6.3 Vicker's Hardness

ANOVA tests were conducted for samples printed with varying parameters and subjected to the same heat treatment in stages. This section will examine the differences or similarities between Vickers hardness among samples built with laser powers 350W, 750W, 1070W, 2000W, and 2620W given separate heat treatments, including stress relieving, HIP-ing, solutionizing, and double aging. A significance level of 0.005 was determined for each group. The first group analyzed was the as-built samples printed with varying parameters where the p-value equaled 0.419 and the F-value equaled 1.02. This is an important finding as it proves that all hardness means are equal for as-built samples printed with varying parameters. Additionally, Fig. 45 shows Turkey's significance plots for AB, SR, HIP, SOL, and aged samples printed with different parameters. Based on these plots, we can conclude that all means are equal for SR, SOL, and aged samples throughout, with p-values of 0.226, 0.015, and 0.515, respectively. However, HIP samples failed to reach significance with a 0.003 p-value and a 5.89 F-value.

Based on these results, it can be concluded that as-built samples have similar Vickers hardness and that SR, SOL, and aging homogenize the hardness values of samples produced with different parameters. However, HIP samples failed to pass the null hypothesis.

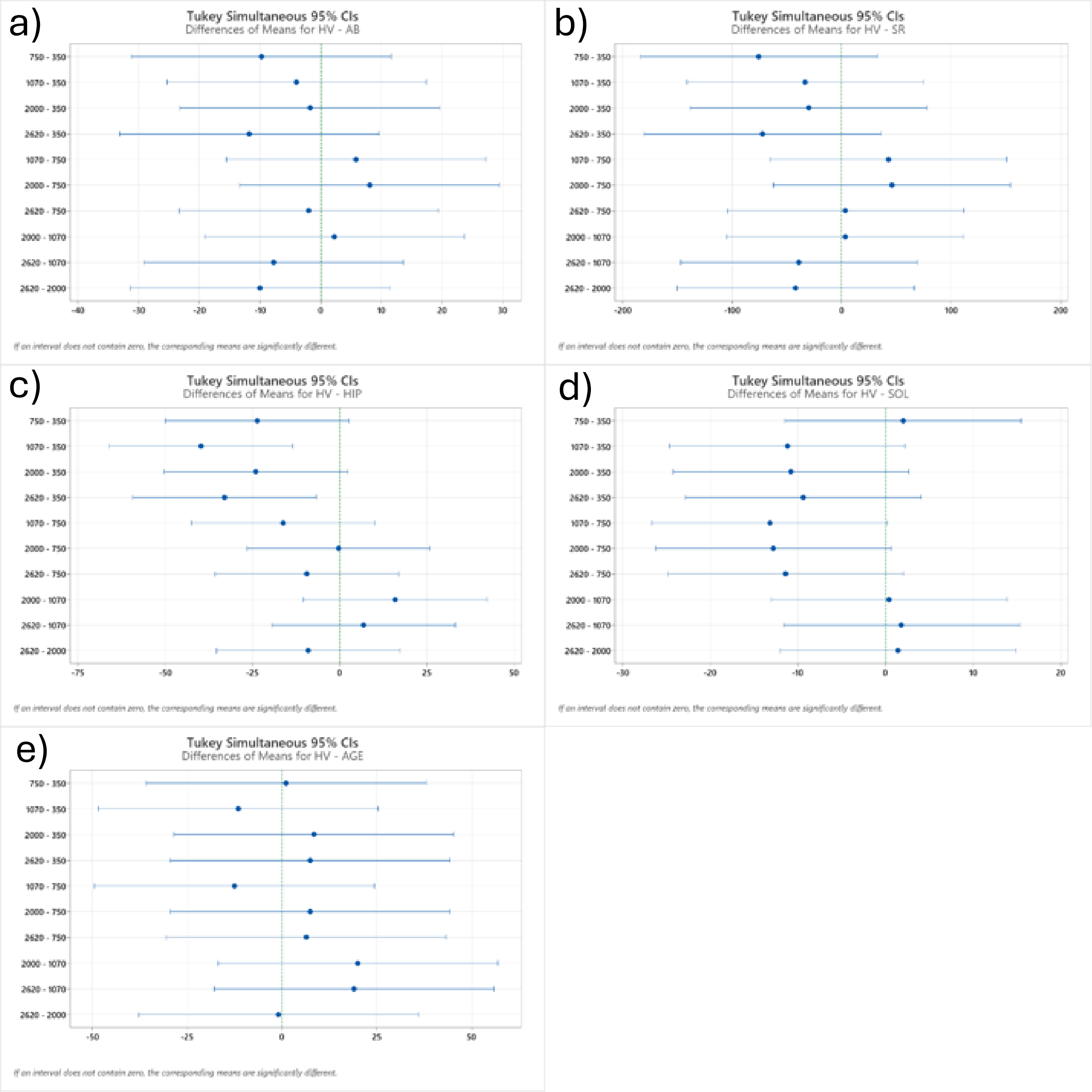

Figure 47. Turkey's significance level test plots for AB, SR, HIP, SOL, and aged samples printed with varying parameters

4.6.4 Grain Size

Statistical analysis was performed on the grain size averages of samples printed with varying parameters subjected to SR, HIP, SOL, and aging heat treatment.

ANOVA tests were performed for each heat treatment, and a significance level 0.05 was determined for each. This test proved all means are not equal, with p-values of 0.042, 0.001, and 0.000 for SR, HIP, and SOL, respectively. However, aged samples achieved a p-value of 0.400.

Fig. 48 shows the interval plots per each heat treatment. From these plots, it can be observed that samples built with a lower laser power generally have a smaller grain size and that grain size increases as laser power increases. Moreover, it is noticeable that as heat treatment advances, anisotropy decreases, and all means across varying parameters are equal by the aging stage. Lastly, Fig. 48 shows how, as heat treatment advances, grain size decreases, which further backs as evidence for the microhardness data seen prior.

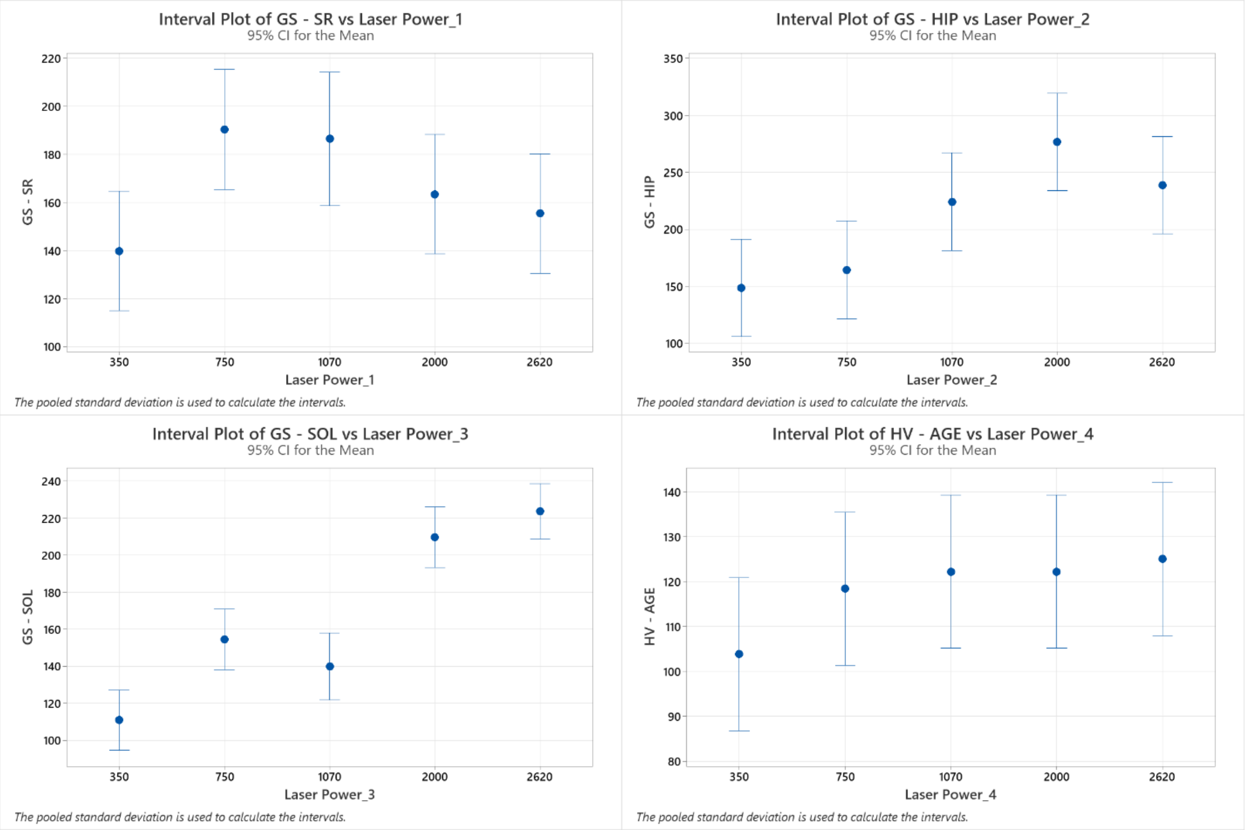

Figure 48. Interval plots for grain size across heat treatments and varying parameters

CHAPTER 5: CONCLUSIONS

Processing can be tuned to tailor desired properties for specific applications, in this way, the materials paradigm is fulfilled. In the case of this study, Inconel 718 samples of the same thickness underwent processing with varying parameters to study the difference between these. However, as built samples consisted of dendritic morphologies which are undesirable in service. HT was performed to further tune the microstructure and thus the properties of DED Inc 718. SOL-age treatment was performed on all samples to enable precipitation of strengthening precipitates to promote strength and creep resistance for aerospace applications.

This study investigated the mechanical properties of 30 tensile and fatigue samples combined and printed with different parameters, including laser power, travel speed, and powder flow rate, each represented by 350W, 750W, 1070W, 2000W, and 2620W. A heat treatment schedule consisting of stress relief annealing (SR), HZ, or HIP at 1165°C for 3 hours, solution treatment (ST) at 1065°C for one hour, and double aging as per NASA’s standard Inconel 718 cycle was performed on all tensile and fatigue samples as well as to a witness sample to study the effects of this at each stage. Fifteen tensile samples were evaluated for 0.2 offset yield stress (YS), ultimate tensile strength (UTS), and elongation (%). Moreover, 15 fatigue samples were tested for low cycle fatigue at a strain range of 1% and a frequency of 0.5Hz. One square mechanical rod or witness sample was built per laser power and sectioned into five cubes. Each witness sample included an NHT section, SR section, HIP section, ST section, and aged section. The defects, microstructures, and hardness values (HV) were investigated for each stage of the HT.

Optical microscopy was utilized to characterize a wide range of microstructures, and SEM imaging was used to compare corresponding fracture surfaces for tensile and fatigue specimens. A density of over 99.5% was achieved for all NHT samples; the percent defect area decreased as heat treatment advanced. In the aged condition, all samples surpassed 99.96% density. The microstructures for every laser power were compared at each stage. Regardless of the laser power, all NHT specimens along the build direction consisted of columnar dendritic morphology, which recrystallized upon heat treatment. Equiaxed grains with twin boundaries and varying sizes from ~104-176µm were observed throughout the various micrographs. Hardness values varied with varying heat treatments; however, they followed a similar trend regardless of laser power. All HV values increased ~69% from the NHT to the aged condition. The HV for sample 350W in the NHT condition was 273HV; after aging, it increased to 463HV.

The corresponding SEM fracture surface imaging showed ductile fracture for all laser powers with ductile features such as dimples and microvoid coalescence ranging between ~1.9-4µm. Low cycle fatigue fracture surface exhibited explicit initiation, propagation, and final fracture stages. The propagation stage was characterized by extensive "river marks," which indicated crack growth direction and were perpendicular to the applied load. Moreover, the final fracture of all samples exhibited ductile fracture features such as dimpling and microvoids.

Specific conclusions that can be drawn from this research are:

- Melt pool size increased with increasing laser power as expected.
- Cooling rates slowed down as laser power increased.
- Density for samples printed with varying parameters (350W-2620W) in the NHT condition achieved densities in the range of ~99.5-99.95%. Upon ST and aging all densities were higher than 99.96%.
- All samples regardless of different parameters showed a dendritic morphology in the as built condition.
- All samples regardless of different parameters underwent recrystallization and growth upon HT yielding a final equiaxed microstructure with grain sizes ranging from ~104-146µm.
- Sample printed with parameter set 350W exhibited the finest microstructure.
- Yield stresses varied from 1100-1138MPa. Specimens built with parameter sets 1070 and 2620 have similar yield strengths However,

there is only a difference of less than 3.4% overall and all values are equal or superior to the wrought material's properties.

- Ultimate tensile strengths varied from 1311-1369MPa with elongations from 23.7-25.6%. Samples 750W and 2620W and 1070W and 2000W have statistically similar UTS'. However, there is only a percent difference of less than 4.3% overall and all values are equal or superior to the wrought material's properties.
- Samples printed with 350W, 750W, 1070W, 2000W, and 2620W all had statistically similar fatigue lives.
- Samples printed with parameter set 350W exhibited overall better properties than others with the smallest grain width highest UTS, and YS.

REFERENCES

[1] De Bartolomeis, Andrea, Stephen T. Newman, I. S. Jawahir, Dirk Biermann, and Alborz Shokrani. "Future Research Directions in the Machining of Inconel 718." *Journal of materials processing technology* 297, (2021): 117260.

[2] Hosseini, E., and V. A. Popovich. "A Review of Mechanical Properties of Additively Manufactured Inconel 718." *Additive manufacturing* 30, (2019): 100877.

[3] Blakey-Milner, Byron, Paul Gradl, Glen Snedden, Michael Brooks, Jean Pitot, Elena Lopez, Martin Leary, Filippo Berto, and Anton du Plessis. "Metal Additive Manufacturing in Aerospace: A Review." *Materials & design* 209, (2021): 110008.

[4] Xing Peng, Lingbao Kong, Jerry Ying, and Hao Wan. “A Review of Post-Processing Technologies in Additive Manufacturing.” *Journal of manufacturing and materials processing. (2021)*

[4] Manjaiah, M., K. Raghavendra, N. Balashanmugam, J. Paulo Davim, and J. Paulo Davim. "Basic Principles of Additive Manufacturing: Different Additive Manufacturing Technologies." In *Additive Manufacturing.* United Kingdom: Elsevier Science & Technology, 2021, 17.

[5] Wong, Kaufui V., and Aldo Hernandez. "A Review of Additive Manufacturing." *ISRN Mechanical Engineering* 2012, (2012): 1-10.

[6] Huang, Jigang, Qin Qin, and Jie Wang. "A Review of Stereolithography: Processes and Systems." *Processes* 8, no. 9 (2020): 1138.

[7] Olayan, H.B.; Hami, H.S.; Owen, E.D. Photochemical and Thermal Crosslinking of Polymers. *J. Macromol. Sci. Part C Polym. Rev.* **1996**, *36*, 671–719.

[8] Bove, Alessandro, Flaviana Calignano, Manuela Galati, and Luca Iuliano. "Photopolymerization of Ceramic Resins by Stereolithography Process: A Review." *Applied sciences* 12, no. 7 (2022): 3591.

[9] Fischer, Nathan A., Alex L. Robinson, Thomas J. Lee, Thomas M. Calascione, Lucas Koerner, and Brittany B. Nelson-Cheeseman. "Magnetic Annealing of Extruded Thermoplastic Magnetic Elastomers for 3D-Printing Via FDM." *Journal of magnetism and magnetic materials* 553, (2022): 169266.

[10] Parandoush, Pedram, and Dong Lin. "A Review on Additive Manufacturing of Polymer-Fiber Composites." *Composite structures* 182, (2017): 36-53.

[11] Patpatiya, Parth, Kailash Chaudhary, Anshuman Shastri, and Shailly Sharma. *A Review on Polyjet 3D Printing of Polymers and Multi-Material Structures.* SAGE Publications, 2022.

[12] Sefene, Eyob Messele. "State-of-the-Art of Selective Laser Melting Process: A Comprehensive Review." *Journal of manufacturing systems* 63, (2022): 250-274.

[13] Oliveira, J. P., A. D. LaLonde, and J. Ma. "Processing Parameters in Laser Powder Bed Fusion Metal Additive Manufacturing." *Materials & design* 193, no. C (2020): 108762.

[14] Dev Singh, D., T. Mahender, and Avala Raji Reddy. "Powder Bed Fusion Process: A Brief Review." *Materials today : proceedings* 46, (2021): 350-355.

[15] Murr, Lawrence E., Sara M. Gaytan, Diana A. Ramirez, Edwin Martinez, Jennifer Hernandez, Krista N. Amato, Patrick W. Shindo, Francisco R. Medina, and Ryan B. Wicker. *Metal Fabrication by Additive Manufacturing using Laser and Electron Beam Melting Technologies.* Elsevier BV, 2012.

[16] Gokuldoss, Prashanth Konda, Sri Kolla, and Jürgen Eckert. *Additive Manufacturing Processes: Selective Laser Melting, Electron Beam Melting and Binder Jetting—Selection Guidelines.* MDPI AG, 2017.

[17] Körner, C. "Additive Manufacturing of Metallic Components by Selective Electron Beam Melting - a Review." *International materials reviews* 61, no. 5 (2016): 361-377.

[18] Li, Ming, Wenchao Du, Alaa Elwany, Zhijian Pei, and Chao Ma. *Metal Binder Jetting Additive Manufacturing: A Literature Review*.

[19] Li, Zuo, Jing Chen, Shang Sui, Chongliang Zhong, Xufei Lu, and Xin Lin. "The Microstructure Evolution and Tensile Properties of Inconel 718 Fabricated by High-Deposition-Rate Laser Directed Energy Deposition." *Additive manufacturing* 31, (2020): 100941.

[20] Svetlizky, David, Mitun Das, Baolong Zheng, Alexandra L. Vyatskikh, Susmita Bose, Amit Bandyopadhyay, Julie M. Schoenung, Enrique J. Lavernia, and Noam Eliaz. "Directed Energy Deposition (DED) Additive Manufacturing: Physical Characteristics, Defects, Challenges and Applications." *Materials today (Kidlington, England)* 49, (2021): 271-295.

[21] Liu, F. Q., L. Wei, S. Q. Shi, and H. L. Wei. "On the Varieties of Build Features during Multi-Layer Laser Directed Energy Deposition." *Additive manufacturing* 36, (2020): 101491.

[22] Tan Zhi’En, Eddie, John Hock Lye Pang, and Jacek Kaminski. "Directed Energy Deposition Build Process Control Effects on Microstructure and Tensile Failure Behaviour." *Journal of materials processing technology* 294, (2021): 117139.

[23] Sampson, Robert, Robert Lancaster, Mark Sutcliffe, David Carswell, Carl Hauser, and Josh Barras. "The Influence of Key Process Parameters on Melt Pool Geometry in Direct Energy Deposition Additive Manufacturing Systems." *Optics and laser technology* 134, (2021): 106609.

[24] Feenstra, D. R., R. Banerjee, Hamish Fraser, A. Huang, A. Molotnikov, and Nick Birbilis. "Critical Review of the State of the Art in Multi-Material Fabrication Via Directed Energy Deposition." 25, no. 4 (2021).

[25] Harter, Isaac. *ŽZ Z1 Attorney.*

[26] Thompson, Scott M., Linkan Bian, Nima Shamsaei, and Aref Yadollahi. "An Overview of Direct Laser Deposition for Additive Manufacturing; Part I: Transport Phenomena, Modeling and Diagnostics." *Additive manufacturing* 8, (2015): 36-62.

[27] Lewis, G K, and Milewski, J.O. Nemec, R.B.. 1997. "Directed light fabrication--a laser metal deposition process for fabrication of near-net shape components". United States. https://doi.org/10.2172/534514. https://www.osti.gov/servlets/purl/534514.

[28] Izadi, Mojtaba, Aidin Farzaneh, Mazher Mohammed, Ian Gibson, and Bernard Rolfe. "A Review of Laser Engineered Net Shaping (LENS) Build and Process Parameters of Metallic Parts." *Rapid prototyping journal* 26, no. 6 (2020): 1059-1078.

[29] Simchi, A. "Direct Laser Sintering of Metal Powders: Mechanism, Kinetics and Microstructural Features." *Materials science & engineering. A, Structural materials : properties, microstructure and processing* 428, no. 1 (2006): 148-158.

[30] Yin, H., and S. D. Felicelli. "Dendrite Growth Simulation during Solidification in the LENS Process." *Acta materialia* 58, no. 4 (2010): 1455-1465.

[31] Stavropoulos, Panagiotis, Harry Bikas, and Theodoros Bekiaris. "A Powder Delivery System for Large-Scale DED Machines." *Procedia CIRP* 109, (2022): 617-622.

[32] Gibson, Ian, David Rosen, and Brent Stucker. *Additive Manufacturing Technologies : 3D Printing, Rapid Prototyping, and Direct Digital Manufacturing.* 2nd ed. 2015 ed. New York, NY: Springer New York, 2015.

[33] Zuo Li, Shang Sui, Xu Ma, Hua Tan, Chongliang Zhong, Guijun Bi, Adam. Clare, Andres Gasser, Jing Chen"High Deposition Rate Powder- and Wire-Based Laser Directed Energy
Deposition of Metallic Materials: A Review". *International Journal of Machine Tools and Manufacture.*

[34] Singh, Ambrish, Sajan Kapil, and Manas Das. "A Comprehensive Review of the Methods and Mechanisms for Powder Feedstock Handling in Directed Energy Deposition." *Additive manufacturing* 35, (2020): 101388.

[35] Terrassa, Katherine L., James C. Haley, Benjamin E. MacDonald, and Julie M. Schoenung. "Reuse of Powder Feedstock for Directed Energy Deposition." *Powder technology* 338, no. C (2018): 819-829.

[36] Anderson, Iver E., Emma M. H. White, and Ryan Dehoff. "Feedstock Powder Processing Research Needs for Additive Manufacturing Development." *Current opinion in solid state & materials science* 22, no. 1 (2018): 8-15.

[37] Ahn, Dong-Gyu. "Directed Energy Deposition (DED) Process: State of the Art." *International Journal of Precision Engineering and Manufacturing - Green Technology* 8, no. 2 (2021): 703-742.

[38] Gradl, Paul. *Principles of Directed Energy Deposition for Aerospace Applications Introduction and Agenda.* 2021.

[39] Lalegani Dezaki, Mohammadreza, Ahmad Serjouei, Ali Zolfagharian, Mohammad Fotouhi, Mahmoud Moradi, M. K. A. Ariffin, and Mahdi Bodaghi. "A Review on Additive/Subtractive Hybrid Manufacturing of Directed Energy Deposition (DED) Process." *Advanced Powder Materials* 1, no. 4 (2022): 100054.

[40] Piscopo, Gabriele, and Luca Iuliano. "Current Research and Industrial Application of Laser Powder Directed Energy Deposition." *International journal of advanced manufacturing technology* 119, no. 11-12 (2022): 6893-6917.

[41] Haley James, Faraone Kevin, Gibson Brian, Simpson Joseph, Dehoff Ryan. *Review of Advanced Manufacturing Techniques and Qualification Processes for Light-Water Reactors: Laser-Directed Energy Deposition Additive Manufacturing* . Oak Ridge National Laboratory, 2021.

[42] Li, C., Z. Y. Liu, X. Y. Fang, and Y. B. Guo. "Residual Stress in Metal Additive Manufacturing." *Procedia CIRP* 71, (2018): 348-353.

[43] Mercelis, Peter, and Jean-Pierre Kruth. "Residual Stresses in Selective Laser Sintering and Selective Laser Melting." *Rapid prototyping journal* 12, no. 5 (2006): 254-265.

[44] Shiomi, M., K. Osakada, K. Nakamura, T. Yamashita, and F. Abe. "Residual Stress within Metallic Model made by Selective Laser Melting Process." *CIRP annals* 53, no. 1 (2004): 195-198.

[45] Mahmood, Muhammad Arif, Diana Chioibasu, Asif Ur Rehman, Sabin Mihai, and Andrei C. Popescu. "Post-Processing Techniques to Enhance the Quality of Metallic Parts Produced by Additive Manufacturing." *Metals (Basel)* 12, no. 1 (2022): 77.

[46] Kumara, Chamara, Andreas Segerstark, Fabian Hanning, Nikhil Dixit, Shrikant Joshi, Johan Moverare, and Per Nylén. "Microstructure Modelling of

Laser Metal Powder Directed Energy Deposition of Alloy 718." *Additive manufacturing* 25, (2019): 357-364.

[47] Li, Zuo, Xu Ma, Chongliang Zhong, Shang Sui, Andres Gasser, and Jing Chen. "Microstructure Homogeneity and Mechanical Property Improvement of Inconel 718 Alloy Fabricated by High-Deposition-Rate Laser Directed Energy Deposition." *Materials science & engineering. A, Structural materials : properties, microstructure and processing* 832, (2022): 142430.

[48] Shamsaei, Nima, Aref Yadollahi, Linkan Bian, and Scott M. Thompson. "An Overview of Direct Laser Deposition for Additive Manufacturing; Part II: Mechanical Behavior, Process Parameter Optimization and Control." *Additive manufacturing* 8, (2015): 12-35.

[49] Zhao, Xiaoming, Jing Chen, Xin Lin, and Weidong Huang. "Study on Microstructure and Mechanical Properties of Laser Rapid Forming Inconel 718." *Materials science & engineering. A, Structural materials : properties, microstructure and processing* 478, no. 1 (2008): 119-124.

[50] *VDM ® Alloy 718 Nicrofer 5219 Nb.* 2020.

[51] Nguyen, Quy Bau, Mui Ling Sharon Nai, Zhiguang Zhu, Chen-Nan Sun, Jun Wei, and Wei Zhou. "Characteristics of Inconel Powders for Powder-Bed Additive Manufacturing." *Engineering* 3, no. 5 (2017): 695-700.

[52] Abu-Lebdeh, Taher M., Genaro Pérez-de León, Sameer A. Hamoush, Roland D. Seals, and Vincent E. Lamberti. "Gas Atomization of Molten Metal: Part II. Applications." *American journal of engineering and applied sciences* 9, no. 2 (2016): 334-349.

[53] Bontha, Srikanth, Nathan W. Klingbeil, Pamela A. Kobryn, and Hamish L. Fraser. "Thermal Process Maps for Predicting Solidification Microstructure in Laser Fabrication of Thin-Wall Structures." *Journal of materials processing technology* 178, no. 1 (2006): 135-142.

[54] ANTONSSON, T., and H. FREDRIKSSON. "The Effect of Cooling Rate on the Solidification of INCONEL 718." *Metallurgical and materials transactions. B, Process metallurgy and materials processing science* 36, no. 1 (2005): 85-96.

[55] Popovich, V. A., E. V. Borisov, A. A. Popovich, V. Sh Sufiiarov, D. V. Masaylo, and L. Alzina. "Impact of Heat Treatment on Mechanical Behaviour of Inconel 718 Processed with Tailored Microstructure by Selective Laser Melting." *Materials & Design* 131, (2017): 12-22.

[56] Newell, David J., Wright-Patterson Air, Force Base, and Ohio . *Solution Anneal Heat Treatment to Enhance Mechanical Performance of Additively Manufactured In718 Dissertation Air Force Institute of Technology.*

[57] SAE International (2016). AMS5662: UNS N07718 1775 ◦F (968 ◦C) Solution Heat Treated, Precipitation Hardenable.

[58] Kouraytem, Nadia, John Varga, Behnam Amin-Ahmadi, Hadi Mirmohammad, Raphaël A. Chanut, Ashley D. Spear, and Owen T. Kingstedt. "A Recrystallization Heat-Treatment to Reduce Deformation Anisotropy of Additively Manufactured Inconel 718." *Materials & design* 198, (2021): 109228.

[59] Elahinia, Mohammad, Narges Shayesteh Moghaddam, Mohsen Taheri Andani, Amirhesam Amerinatanzi, Beth A. Bimber, and Reginald F. Hamilton. "Fabrication of NiTi through Additive Manufacturing: A Review." *Progress in materials science* 83, (2016): 630-663.

[60] Wang, Xiaoqing, and Kevin Chou. "The Effects of Stress Relieving Heat Treatment on the Microstructure and Residual Stress of Inconel 718 Fabricated by Laser Metal Powder Bed Fusion Additive Manufacturing Process." *Journal of manufacturing processes* 48, (2019): 154-163.

[61] ASTM International (2014). ASTM F3055-14a: Standard Specification for Additive Manufacturing Nickel Alloy (UNS N07718) with Powder Bed Fusion. *Annual Book of ASTM Standards*, pages 1–8

[62] Soltani-Tehrani, Arash, Poshou Chen, Colton Katsarelis, Paul Gradl, Shuai Shao, and Nima Shamsaei. "Laser Powder Directed Energy Deposition (LP-DED) NASA HR-1 Alloy: Laser Power and Heat Treatment Effects on Microstructure and Mechanical Properties." *Additive manufacturing letters* 3, (2022): 100097.

[63] Cao, Yu, Pucun Bai, Fei Liu, Xiaohu Hou, and Yuhao Guo. *Effect of the Solution Temperature on the Precipitates and Grain Evolution of IN718 Fabricated by Laser Additive Manufacturing.* MDPI AG, 2020.

[64] González-Velázquez, Jorge Luis. *Fractography and Failure Analysis.* 1st ed. 2018 edition. ed. Cham: Springer International Publishing, 2018.

[65] Ase, David, and Filip Anderfelt. "Methodology for Obtaining S-N Curves using Fatigue Testing and Static FEA." Jönköping University, 2022.

[66] Denny, J., A. N. Jinoop, C. P. Paul, R. Singh, and K. S. Bindra. "Fatigue Crack Propagation Behaviour of Inconel 718 Structures Built using Directed Energy Deposition Based Laser Additive Manufacturing." *Materials letters* 276, (2020): 128241.

[67] Johnson, Alex S., Shuai Shao, Nima Shamsaei, Scott M. Thompson, and Linkan Bian. "Microstructure, Fatigue Behavior, and Failure Mechanisms of Direct Laser-Deposited Inconel 718." *JOM (1989)* 69, no. 3 (2017): 597-603.

[68] Kelley, Paul. "Fatigue Behavior of Direct Metal Laser Sintered (DMLS) Inconel 718." Tufts University, 2016.

[69] Konečná, Radomila, Gianni Nicoletto, Ludvík Kunz, and Adrián Bača. "Microstructure and Directional Fatigue Behavior of Inconel 718 Produced by Selective Laser Melting." *Procedia Structural Integrity* 2, (2016): 2381-2388.

[70] Aydinöz, M. E., F. Brenne, M. Schaper, C. Schaak, W. Tillmann, J. Nellesen, and T. Niendorf. "On the Microstructural and Mechanical Properties of Post-Treated Additively Manufactured Inconel 718 Superalloy Under Quasi-Static and Cyclic Loading." *Materials science & engineering. A, Structural materials : properties, microstructure and processing* 669, (2016): 246-258.

[71] Gribbin, Sean, Jonathan Bicknell, Luke Jorgensen, Igor Tsukrov, and Marko Knezevic. "Low Cycle Fatigue Behavior of Direct Metal Laser Sintered Inconel Alloy 718." *International journal of fatigue* 93, (2016): 156-167.

[72] Pratheesh Kumar, S., S. Elangovan, R. Mohanraj, and J. R. Ramakrishna. "A Review on Properties of Inconel 625 and Inconel 718 Fabricated using Direct Energy Deposition." *Materials today : proceedings* 46, (2021): 7892-7906.

[73] Farber, Bryton, Kathryn A. Small, Christopher Allen, Robert J. Causton, Ashley Nichols, John Simbolick, and Mitra L. Taheri. "Correlation of Mechanical Properties to Microstructure in Inconel 718 Fabricated by Direct Metal Laser

Sintering." *Materials science & engineering. A, Structural materials : properties, microstructure and processing* 712, (2018): 539-547.

[74] Chlebus, E., K. Gruber, B. Kuźnicka, J. Kurzac, and T. Kurzynowski. "Effect of Heat Treatment on the Microstructure and Mechanical Properties of Inconel 718 Processed by Selective Laser Melting." *Materials science & engineering. A, Structural materials : properties, microstructure and processing* 639, (2015): 647-655.

[75] Wang, Zemin, Kai Guan, Ming Gao, Xiangyou Li, Xiaofeng Chen, and Xiaoyan Zeng. "The Microstructure and Mechanical Properties of Deposited-IN718 by Selective Laser Melting." *Journal of alloys and compounds* 513, (2012): 518-523.

[76] Soltani-Tehrani, Arash, Poshou Chen, Colton Katsarelis, Paul Gradl, Shuai Shao, and Nima Shamsaei. "Mechanical Properties of Laser Powder Directed Energy Deposited NASA HR-1 Superalloy: Effects of Powder Reuse and Part Orientation." *Thin-walled structures* 185, (2023): 110636.

[77] Zhang, Peng, Qiang Zhu, Chao Hu, Chuan-jie Wang, Gang Chen, and He-yong Qin. "Cyclic Deformation Behavior of a Nickel-Base Superalloy Under Fatigue Loading." *Materials in engineering* 69, (2015): 12-21.

[78] ISO/ASTM, Additive Manufacturing - General Principles Terminology (ASTM52900), 2015. https://www.iso.org/standard/69669.html.

[79] Najmon JC, Raeisi S, Tovar A (2019) Review of additive manufacturing technologies and applications in the aerospace industry.

[80] I. Yadroitsev, I. Yadriotsava, A. du Plessis, E. MacDonald, Fundamentals of Laser Powder Bed Fusion of Metals, first ed. 2021. [Online]. Available: https://www.elsevier.com/books/fundamentals-of-laser-powder-bed-fusion-of-metals/yadroitsev/978-0-12-824090-8.

[81] Babuska TF, Krick BA, Susan DF, Kustas AB (2021) Comparison of powder bed fusion and directed energy deposition for tailoring mechanical properties of traditionally brittle alloys. 28:30

[82] Terrassa KL, Haley JC, MacDonald BE, Schoenung JM (2018) Reuse of powder feedstock for directed energy deposition. 338(C):819–829. https://doi.org/10.1016/j.powtec.2018.07.065

[83] Madhavadas V, Srivastava D, Chadha U, Aravind Raj S, Sultan MTH, Shahar FS, Shah AUM (2022) A review on metal additive manufacturing for intricately shaped aerospace components. 39:18

[84] Martin, A. A., Calta, N. P., Khairallah, S. A., Wang, J., Depond, P. J., Fong, A. Y., Thampy, V., Guss, G. M., Kiss, A. M., Stone, K. H., Tassone, C. J., Nelson Weker, J., Toney, M. F., Van Buuren, T., & Matthews, M. J. (2019). *Dynamics of*

pore formation during laser powder bed fusion additive manufacturing. Springer Science and Business Media LLC. 10.1038/s41467-019-10009-2

[85] Alqawasmi, L., Bijjala, S. T., Khraishi, T., & Kumar, P. (2023). *Mechanical property heterogeneity in inconel 718 superalloy manufactured by directed energy deposition*. Springer Science and Business Media LLC. 10.1007/s10853-023-09249-x

[86] Mueller, M., Franz, K., Riede, M., López, E., Brueckner, F., & Leyens, C. (2023). *Influence of process parameter variation on the microstructure of thin walls made of inconel 718 deposited via laser-based directed energy deposition with blown powder*. Springer Science and Business Media LLC. 10.1007/s10853-023-08706-x

[87] Zhong, C., Chen, J., Linnenbrink, S., Gasser, A., Sui, S., & Poprawe, R. (2016). *A comparative study of inconel 718 formed by high deposition rate laser metal deposition with GA powder and PREP powder*. Elsevier BV. 10.1016/j.matdes.2016.06.037

[88] S. Azadian, L.-Y. Wei, R. Warren (2004) Delta phase precipitation in inconel 718, Mater. Charact. 53 (1) 7–16.

[89] Ramiro, P., Galarraga, H., Pérez-Checa, A., Ortiz, M., Alberdi, A., Bhujangrao, T., Morales, E., & Ukar, E. (2022). *Effect of heat treatment on the microstructure and hardness of ni-based alloy 718 in a variable thickness*

geometry deposited by powder fed directed energy deposition. MDPI AG. 10.3390/met12060952

[90] Zhang, D., Niu, W., Cao, X., & Liu, Z. (2015). *Effect of standard heat treatment on the microstructure and mechanical properties of selective laser melting manufactured inconel 718 superalloy*. Elsevier BV. 10.1016/j.msea.2015.06.021

[91] Jardon, Z., Ertveldt, J., Lecluyse, R., Hinderdael, M., & Pyl, L. (2022). *Directed energy deposition roughness mitigation through laser remelting*. Elsevier BV. 10.1016/j.procir.2022.08.042

[92] Kim, F. H., & Moylan, S. P. (2018). *Literature review of metal additive manufacturing defects*. National Institute of Standards and Technology. 10.6028/nist.ams.100-16

[93] Frisk, Andersson, & Rogberg. (2019). Cast structure in alloy A286, an iron-nickel based superalloy. MDPI AG. 10.3390/met9060711

[94] Alin, A. (2010). Minitab. Wiley. 10.1002/wics.113

[95] Henson, R. N. (2015). Analysis of variance (ANOVA). Elsevier. 10.1016/b978-0-12-397025-1.00319-5

[96] Nanda, A., Mohapatra, D. B. B., Mahapatra, A. P. K., Mahapatra, A. P. K., & Mahapatra, A. P. K. (2021). Multiple comparison test by tukey’s honestly

significant difference (HSD): Do the confident level control type I error. AkiNik Publications. 10.22271/maths.2021.v6.i1a.636

[97] Rogalsky, A., Rishmawi, I., Brock, L., & Vlasea, M. (2018). *Low cost irregular feed stock for laser powder bed fusion*. Elsevier BV. 10.1016/j.jmapro.2018.08.032

[98] Verhoef, L. A., Budde, B. W., Chockalingam, C., García Nodar, B., & Van Wijk, A. J. M. (2017). The effect of additive manufacturing on global energy demand: An assessment using a bottom-up approach. Elsevier BV. 10.1016/j.enpol.2017.10.034

[99] Vafadar, A., Guzzomi, F., Rassau, A., & Hayward, K. (2021). Advances in metal additive manufacturing: A review of common processes, industrial applications, and current challenges. MDPI AG. 10.3390/app11031213

[100] Sreekanth, S., Hurtig, K., Joshi, S., & Andersson, J. (2022). Effect of process parameters and heat treatments on delta-phase precipitation in directed energy deposited alloy 718. Springer Science and Business Media LLC. 10.1007/s40194-022-01253-0

[101] Tham, N. Y. S., Tay, G. R. S., Yao, B., Wu, K., & Dong, Z. (2023). Effect of aging parameters on inconel 718 fabricated by laser directed energy deposition. Elsevier BV. 10.1016/j.cjmeam.2023.100101

[102] Dos Santos Paes, L. E., Pereira, M., Xavier, F. A., Weingaertner, W. L., & Vilarinho, L. O. (2021). Lack of fusion mitigation in directed energy deposition with laser (DED-L) additive manufacturing through laser remelting. Elsevier BV. 10.1016/j.jmapro.2021.10.052

[103] AWS. Standard welding terms and definitions – AWS A3.0M/A3.0. AWS; 2010.

[104] Kobryn PA, Moore EH, Semiatin. The effect of laser power and traverse speed on microstructure, porosity and build height in laser-deposited Ti-6Al-4V. Scr Mater 2000;43:299–305.

[105] Dass, A., & Moridi, A. (2019). State of the art in directed energy deposition: From additive manufacturing to materials design. MDPI AG. 10.3390/coatings9070418

CURRICULUM VITA

Dana Godinez earned her Bachelor of Science in Metallurgical and Materials Engineering in December 2022 from the University of Texas at El Paso. During this time, she had the privilege of joining the W.M. Keck Center for 3D Innovation at El Paso where she earned her skills in additive manufacturing and materials characterization. In 2023 Dana got accepted to the Master’s program in Metallurgical and Material Science Engineering. To this day she has earned the opportunity to work with important aerospace companies such as NASA and the ARL.

Contact information: dvgodinez@miners.utep.edu

This thesis was typed by Dana Godinez